



This discussion paper is/has been under review for the journal Geoscientific Model Development (GMD). Please refer to the corresponding final paper in GMD if available.

Quantifying the impact of sub-grid surface wind variability on sea salt and dust emissions in CAM5

K. Zhang¹, C. Zhao¹, H. Wan¹, Y. Qian¹, R. C. Easter¹, S. J. Ghan¹,
K. Sakaguchi¹, and X. Liu²

¹Pacific Northwest National Laboratory, Richland, WA, USA

²University of Wyoming, Laramie, WY, USA

Received: 13 July 2015 – Accepted: 4 August 2015 – Published: 27 August 2015

Correspondence to: K. Zhang (kai.zhang@pnnl.gov)

Published by Copernicus Publications on behalf of the European Geosciences Union.

GMDD

8, 7249–7312, 2015

Sub-grid wind-driven aerosol emissions in CAM5

K. Zhang et al.

Title Page

Abstract

Introduction

Conclusions

References

Tables

Figures



Back

Close

Full Screen / Esc

Printer-friendly Version

Interactive Discussion



Abstract

This paper evaluates the impact of sub-grid variability of surface wind on sea salt and dust emissions in the Community Atmosphere Model version 5 (CAM5). The basic strategy is to calculate emission fluxes multiple times, using different wind speed samples of a Weibull probability distribution derived from model-predicted grid-box mean quantities.

In order to derive the Weibull distribution, the sub-grid standard deviation of surface wind speed is estimated by taking into account four mechanisms: turbulence under neutral and stable conditions, dry convective eddies, moist convective eddies over the ocean, and air motions induced by meso-scale systems and fine-scale topography over land. The contributions of turbulence and dry convective eddy are parameterized using schemes from the literature, while the wind variabilities caused by moist convective eddies and fine-scale topography are estimated using empirical relationships derived from an operational weather analysis dataset at 15 km resolution. The estimated sub-grid standard deviations of surface wind speed agree well with reference results derived from one year of global weather analysis at 15 km resolution and from two regional model simulations with 3 km grid spacing.

The wind-distribution-based emission calculations are implemented in CAM5. Simulations at 2° resolution indicate that sub-grid wind variability has relatively small impacts (about 7 % increase) on the global annual mean emission of sea salt aerosols, but considerable influence on the emission of dust. Among the considered mechanisms, dry convective eddies and meso-scale flows associated with topography are major causes of dust emission enhancement. With all the four mechanisms included and without additional adjustment of uncertain parameters in the model, the simulated global and annual mean dust emission increase by about 50 % compared to the default model. By tuning the globally constant dust emission scale factor, the global annual mean dust emission, aerosol optical depth, and top-of-atmosphere radiative fluxes can be adjusted to the level of the default model, but the frequency distribution of dust emis-

Sub-grid wind-driven aerosol emissions in CAM5

K. Zhang et al.

[Title Page](#)

[Abstract](#)

[Introduction](#)

[Conclusions](#)

[References](#)

[Tables](#)

[Figures](#)

◀

▶

◀

▶

[Back](#)

[Close](#)

[Full Screen / Esc](#)

[Printer-friendly Version](#)

[Interactive Discussion](#)



sion changes, with more contribution from weaker wind events and less contribution from stronger wind events.

1 Introduction

Atmospheric aerosols are important modulators of cloud formation processes and the energy budget of the climate system. The physical processes associated with aerosol sources and sinks are often nonlinear. In global and regional general circulation models (GCMs), the variabilities of meteorological fields at scales not resolved by the computational mesh have been found to have direct influences on aerosol formation as well as the subsequent microphysical changes and removal processes (Qian et al., 2010; Stevens and Pierce, 2013). Those sub-grid variabilities (SGV) hence eventually affect the simulated aerosol direct and indirect forcing (e.g. Haywood et al., 1997; Ghan and Easter, 1998; Gustafson et al., 2011).

Among the different species of aerosols, sea salt and dust contribute to a large fraction of the total aerosol burden in the atmosphere (Textor et al., 2006). Substantial discrepancies have been seen in the simulated emission fluxes of these two aerosol types in global aerosol model inter-comparison studies (Textor et al., 2006; Huneeus et al., 2011). Although different parameterization schemes are used in individual models, the near-surface wind speed is always a major factor that affects the emission of sea salt and dust. In most global aerosol models, the emission calculations are based on the grid-box mean near-surface wind speed, or the friction velocity derived from that mean speed, despite the fact that wind speed can have large spatial variabilities inside a typical GCM grid box (100–200 km across each edge). Due to the strongly nonlinear dependence of emission flux on wind speed, emission estimates made solely from GCM grid-box mean quantities can differ considerably from the grid-box average of fluxes estimated at a finer spatial scale (Westphal et al., 1988). It is therefore important to take into account sub-grid wind variabilities when calculating wind-driven aerosol emissions in GCMs.

Title Page	
Abstract	Introduction
Conclusions	References
Tables	Figures
Full Screen / Esc	
Printer-friendly Version	
Interactive Discussion	



Sub-grid wind-driven aerosol emissions in CAM5

K. Zhang et al.

[Title Page](#)

[Abstract](#)

[Introduction](#)

[Conclusions](#)

[References](#)

[Tables](#)

[Figures](#)

[◀](#)

[▶](#)

[◀](#)

[▶](#)

[Back](#)

[Close](#)

[Full Screen / Esc](#)

[Printer-friendly Version](#)

[Interactive Discussion](#)



was used to estimate the grid-box mean wind speed, and the mean speed was used to do a single calculation of the heat, moisture or dust mass flux. For dust emission, considering that the dependency on wind speed is highly nonlinear, several studies have attempted to further remedy the accuracy issue by constructing a frequency distribution of the surface wind speed for the emission calculation. Different types of probability density functions (PDF) were assumed in the dust modeling studies. For example, Marcella and Eltahir (2010) used Gaussian distribution and Cakmur et al. (2004) used double-Gaussian.

In this work, we introduced a sub-grid treatment for the sea salt and dust emission calculation for the Community Atmospheric Model version 5 (CAM5). Like in Cakmur et al. (2004), the contribution of neutral/stable turbulence, dry convective eddies, and moist convective eddies are considered. In addition to these processes, the impact of wind variabilities induced by meso-scale systems and topography-generated gravity waves over land is parameterized with an empirical method. In contrast to Cakmur et al. (2004) and Marcella and Eltahir (2010), the wind PDF is assumed to follow the Weibull distribution (Justus et al., 1979; Pavia and O'Brien, 1986; Monahan, 2006; Carta et al., 2009).

The present paper present materials to answer the following scientific questions for the CAM5 model:

- 20 1. How can we approximate the wind SGV using the grid-box mean physical quantities provided by an atmospheric GCM?
2. How large is the impact of sub-grid variability of surface wind speeds on the grid-box mean aerosol emission?
- 25 3. How does the estimated surface wind SGV affect the sea-salt and dust aerosol distributions and their impact on the top-of-atmosphere energy balance?

In the remainder of the paper, we first introduce the CAM5 model and the formulation of its sea salt and dust emission parameterizations (Sect. 2). We then address the

Title Page	
Abstract	Introduction
Conclusions	References
Tables	Figures
◀	▶
◀	▶
Back	Close
Full Screen / Esc	
Printer-friendly Version	
Interactive Discussion	



three science questions in Sects. 3–5. Each section starts with a description of the methodology and data, then proceeds to a discussion of the results. The conclusions are drawn in Sect. 6.

2 Sea salt and dust emissions in CAM5

- 5 The CAM model used in this study is based on the version 5.3 release, the atmospheric component of the Community Earth System Model version 1.2.0 (<http://www.cesm.ucar.edu/models/cesm1.2/>). We now introduce the basic features of the model configuration (Sect. 2.1), describe the sea salt and dust emission parameterizations (Sects. 2.3 and 2.4), and introduce the strategy used here to include sub-grid
10 wind variability in the emission calculations (Sect. 2.5).

2.1 CAM5 overview

In this study we use CAM5 with the finite-volume dynamical core (Lin, 2004) at 1.9° lat × 2.5° lon horizontal resolution and with 30 vertical layers. The modal aerosol module MAM3 (Liu et al., 2012a) represents the tropospheric aerosol life cycle, including various emission and formation mechanisms, microphysical processes, and removal mechanisms. Six aerosol components are considered in the model, including sulfate, black carbon, primary and secondary organic aerosols, sea salt, and mineral dust. The emission fluxes of sea salt and dust are calculated interactively, while the emissions of other aerosol and precursor gas species are prescribed. The stratiform
15 cloud microphysics in CAM5 is represented by a two-moment parameterization (Morrison and Gettelman, 2008; Gettelman et al., 2008). Aerosols can affect the formation and properties of stratiform clouds by acting as cloud condensation nuclei (CCN) or ice nucleating particles. Deep convection and shallow convection are parameterized using the schemes of Zhang and McFarlane (1995) and Park and Bretherton (2009),
20 respectively. Aerosols do not affect microphysics in convective clouds. Moist turbulence
25

Sub-grid wind-driven aerosol emissions in CAM5

K. Zhang et al.

Title Page

Abstract

Introduction

Conclusions

References

Tables

Figures

◀

▶

◀

▶

Back

Close

Full Screen / Esc

Printer-friendly Version

Interactive Discussion



is represented by the parameterization of Bretherton and Park (2009). Shortwave and longwave radiative transfer calculations are performed using RRTMG (Rapid Radiative Transfer Model for General circulation model applications, Iacono et al., 2008; Mlawer et al., 1997). Processes related to the mass and energy exchanges at the atmosphere-

5 land interface are described by the Community Land Model version 4 (CLM4, Lawrence et al., 2011). Further details of the CAM5 and CLM4 model formulations can be found in Neale et al. (2010) and Oleson et al. (2010), respectively.

2.2 Notation and terminology

In this paper, the symbol $\bar{\psi}$ denotes the average of a generic variable ψ over a GCM 10 grid box, where ψ can be either scalar or vector.

For the horizontal wind vector \mathbf{v} , we use the capital letter U to denote its magnitude (i.e. the wind speed):

$$U \equiv |\mathbf{v}| \equiv \mathbf{v} \cdot \mathbf{v} \equiv \sqrt{u^2 + v^2} \quad (1)$$

Since U is a nonlinear function of \mathbf{v} , the grid-box average of wind speed (i.e., \bar{U}) is larger 15 than the magnitude of the grid-box mean wind vector (i.e., $|\bar{\mathbf{v}}|$), due to the existence of sub-grid wind variation. The estimation of \bar{U} is addressed in Sect. 4 (Eq. 28). Another point to clarify is that throughout the paper, the term “surface wind” is used to refer to the horizontal wind at the lowest model level.

2.3 Sea salt emission scheme

20 The sea salt emission scheme in CAM5 is based on the work of Mårtensson et al. (2003). The emission flux F ($\text{kg m}^{-2} \text{s}^{-1}$) in the default model is calculated as

$$F = [U_{10}(|\bar{\mathbf{v}}|)]^{3.41} A_{\text{ocn}} E \quad (2)$$

where $U_{10}(|\bar{\mathbf{v}}|)$ is the 10 m wind speed diagnosed from $|\bar{\mathbf{v}}|$ without considering the sub-grid wind variability. A_{ocn} is the area fraction of open ocean in the grid box, and E is

Sub-grid wind-driven aerosol emissions in CAM5

K. Zhang et al.

[Title Page](#)

[Abstract](#)

[Introduction](#)

[Conclusions](#)

[References](#)

[Tables](#)

[Figures](#)

◀

▶

◀

▶

[Back](#)

[Close](#)

[Full Screen / Esc](#)

[Printer-friendly Version](#)

[Interactive Discussion](#)



a function of sea surface temperature and the assumed emission size distribution. The detailed expression of E can be found in Supplement of Liu et al. (2012a).

2.4 Dust emission scheme

The parameterization of mineral dust aerosol emission in CAM5 is strongly tied to the land component CLM. CLM considers multiple landunits (vegetated, glacier, wetland, lake, and urban) within a grid box, among which only the vegetated surfaces can emit dust. Using the Dust Entrainment And Deposition (DEAD) model of Zender et al. (2003), it is assumed that dust sources are located in arid or semi-arid marginally-vegetated regions where strong winds can mobilize dust from the surface. The vegetated landunit in CLM is further categorized by plant functional type (PFT, e.g., tropical broadleaf deciduous tree, boreal needleleaf evergreen tree; cf. Table 2.1 in Oleson et al., 2010). The dust emission flux is first calculated for each PFT,¹ then summed up using the area-weighting to give the grid-box average, i.e.,

$$\overline{F} = \sum_j A_j F_j. \quad (3)$$

For the j th PFT of a grid-box, the vertical flux of dust mass emission (unit: $\text{kg m}^{-2} \text{s}^{-1}$) is calculated by

$$F_j = TS\alpha f_m Q_{s_i}. \quad (4)$$

Here T is an adjustable tuning parameter which is time and space invariant. The source erodibility factor S and the sandblasting mass efficiency α are time-invariant but depen-

¹It should be noted that the “bare ground” fraction defined in the original dust emission parameterization is different from the bare ground land surface type defined in CLM. The bare ground fraction decreases linearly as the vegetation area index (LAI + SAI) increases from zero to a prescribed threshold value (Zender et al., 2003). Therefore, even for PFTs that are not bare ground according to the CLM categorization, dust emission is still possible. Furthermore, dust emission is not considered over ice sheets, wetland areas, or lakes in CAM5/CLM4.



dent on geographical location. f_m is the fraction of grid cell area covered by exposed bare soil suitable for dust mobilization. The horizontally saltating mass flux Q_{s_j} is calculated according to White (1979):

$$Q_{s_j} = \begin{cases} \frac{c_s \rho_a u_{*s_j}^3}{g} \left(1 - \frac{u_{*t}}{u_{*s_j}}\right) \left(1 + \frac{u_{*t}}{u_{*s_j}}\right)^2, & u_{*s_j} > u_{*t} \\ 0, & u_{*s_j} \leq u_{*t} \end{cases}, \quad (5)$$

- ⁵ c_s denotes the saltation parameter (time-invariant and globally constant). ρ_a is air density, and g is gravity. The threshold friction velocity u_{*t} is a function of moisture content in the top soil layer (PFT independent). In the default model (i.e., without wind SGV), the PFT-dependent u_{*s_j} is calculated using

$$u_{*s_j} = \begin{cases} u_{*j} + 0.003 U_{10j}^2 \left(1 - \frac{u_{*t}}{u_{*j}}\right)^2 & u_{*j} \geq u_{*t} \\ u_{*j}, & u_{*j} < u_{*t} \end{cases} \quad (6)$$

- ¹⁰ The friction velocity u_{*j} and the 10 m wind speed U_{10j} are functions of surface wind speed, boundary layer stability, and characteristics of the land surface.

Like in earlier studies (e.g., Godfrey and Beljaars, 1991; Lunt and Valdes, 2002), in order to take into account the enhancement of mean wind speed by dry convective eddies, in the default CAM5, the calculation of surface heat, moisture and tracer fluxes over land uses the following approximation for the grid-box mean surface wind speed:

$$\bar{U}_{\text{adj}} = \sqrt{|\bar{\mathbf{v}}|^2 + \sigma_{U,d}^2}. \quad (7)$$

Here $\sigma_{U,d}$ is the standard deviation of sub-grid wind speed associated with dry convective eddy (details are given in Sect. 4.2.2). \bar{U}_{adj} is used in the calculation of U_{10} and u_* , which not only affects Eq. (6) and hence the dust emissions, but also all other flux

Title Page	Abstract	Introduction
Conclusions	References	
Tables	Figures	
◀	▶	
◀	▶	
Back	Close	
Full Screen / Esc		
	Printer-friendly Version	
	Interactive Discussion	



calculations that use U_{10} and u_* over land. On the other hand, the adjustment (Eq. 7) is not applied over the ocean, thus does not affect the sea salt emission in the default model.

2.5 Incorporating surface wind variability in emissions calculations

- 5 Equations (2)–(6) reveal that the parameterized sea salt and dust emissions are directly affected by the 10 m wind U_{10} and the friction velocity u_* , both of which depend on the surface wind speed. In this study, the basic approach to introducing sub-grid scale wind variability in the calculation of aerosol emissions is to (1) assume a Weibull PDF for surface wind speed, and calculate the Weibull PDF parameters from existing model
10 quantities, (2) obtain multiple samples of surface wind speed within each GCM grid box, (3) calculate the sea salt and dust emissions for each sample, and (4) provide the average fluxes to the host GCM.

Using a generic notation, we assume M samples of surface wind speed can be obtained in a GCM grid box (i.e., U_i with $i = 1, \dots, M$), each of which represents an area fraction w_i , and has a corresponding 10 m wind $U_{10,i}$ and a friction velocity $u_{*,i}$. The grid-box mean sea salt emission flux is then calculated by
15

$$\bar{F} = A_{\text{ocn}} E \sum_i w_i U_{10,i}^{3.41}. \quad (8)$$

For dust, we note that the friction velocity u_* is strongly affected by land surface characteristics, which has partially been taken into account (in the default model) by distinguishing different PFTs. This is different from the dust emission parameterization used in many other global aerosol-climate models (e.g. ECHAM5-HAM2 described in Zhang et al., 2012), in which the calculation of the friction velocity often neglects the impact of sub-grid variation of vegetation type. On the other hand, for a single PFT in a grid cell, u_* can still have strong SGV because of the inhomogeneity in surface wind speed. In this study we take multiple surface wind samples ($U_i, i = 1, \dots, M$) for each PFT, calculate $u_{*,Sj,i}$ and $Q_{Sj,i}$ in analogy to Eqs. (6) and (5), respectively, then calculate
20
25

[Title Page](#)

[Abstract](#)

[Introduction](#)

[Conclusions](#)

[References](#)

[Tables](#)

[Figures](#)

[◀](#)

[▶](#)

[◀](#)

[▶](#)

[Back](#)

[Close](#)

[Full Screen / Esc](#)

[Printer-friendly Version](#)

[Interactive Discussion](#)



the grid-box mean dust emission flux as a weighted sum over all PFTs and all surface wind samples, i.e.,

$$\bar{F} = \sum_j A_j \left(\sum_i w_{j,i} F_{j,i} \right). \quad (9)$$

The strategy of doing multiple emission calculations in each grid box is similar to that used by Grini and Zender (2004) and Cakmur et al. (2004), although in our work the wind speed samples are derived differently. The details are explained in Sects. 4 and 5. Before describing the method for estimating sub-grid wind variability, we first present in the next section a diagnostic analysis of the impact of sub-grid wind on aerosol emission, assuming that the sub-grid wind variability is already known.

10 3 Offline estimate of the impact of wind variability

In this section, we address the first science question under the assumption that the sub-grid variability of surface wind is known to sufficiently high accuracy. Applying a method similar to those used in many recent studies on resolution sensitivities of parameterized physical processes (e.g. Arakawa et al., 2011), we use high-resolution wind data and derive the surface wind statistics in imagined grid boxes that are roughly 200 km by 200 km in size.

Two sources of high-resolution data are used. The first dataset contains one year (2011) of the 6 hourly operational analysis from the European Center for Medium-range Weather Forecasts (ECMWF). The horizontal resolution is $T_L 1279$, corresponding to grid spacings of about 15 km. A special advantage of this dataset is its global coverage, which is important for estimating the impact of wind SGV on sea salt emission. Our imagined coarse resolution grid is a 2° lat \times 2° lon mesh. Each grid box overlaps about 200 points on the $T_L 1279$ grid. The averaging from fine-resolution grid points to coarse-resolution boxes uses an area weighting that takes into account fractional contributions of the ECMWF grid cells in each 2° imagined grid box.

[Title Page](#)

[Abstract](#)

[Introduction](#)

[Conclusions](#)

[References](#)

[Tables](#)

[Figures](#)

[◀](#)

[▶](#)

[◀](#)

[▶](#)

[Back](#)

[Close](#)

[Full Screen / Esc](#)

[Printer-friendly Version](#)

[Interactive Discussion](#)



The second wind dataset includes two regional model simulations conducted with the WRF model v3.4.1 (Skamarock and Klemp, 2008) at 3 km resolution: one for October 2008 with a 900 km × 900 km domain centered at 52° S, 145° W over the Southern Ocean, and one for 1–7 April 2011 with a 900 km × 900 km domain centered at 40° N, 85° E over western China near the Taklamakan Desert (Fig. 1). Both simulations used the CAM5 physics suite implemented in WRF by Ma et al. (2014). The meteorological initial conditions and lateral boundary conditions are derived from ECMWF analysis at 6 h intervals. For the calculations discussed in this section and in Sect. 4, each WRF domain is divided into 16 imagined grid boxes of 225 km spacing, and only the 4 inner boxes are used in order to avoid potential impacts of boundary effects on the regional model simulations (Fig. 1b).

A global view of the sub-grid spatial variability of surface wind is presented in Fig. 2 which shows the grid-box mean and sub-grid standard deviation of U_{10} on the 2° coarse mesh. The statistics were first calculated from the 15 km ECMWF data at 6 hourly intervals, then temporally averaged to give the January, July and annual averages. Over the ocean, grid-box mean wind and sub-grid variability are both strong in the storm tracks. In contrast, the trade wind regions have relatively strong winds but weak SGV, while the regions with strong tropical precipitation are associated with weak grid-box mean wind and strong spatial variability. Over land the mean wind is generally low, but there is strong spatial inhomogeneity associated with complex topography (e.g., mountains and coastlines). The contrasts in geographical distribution between the grid-box mean and sub-grid variability indicate that the mean wind alone is not a good predictor of variability.

Based on Eq. (8), the impact of sub-grid wind variability on the parameterized sea salt emission can be estimated by comparing the following two quantities for each grid box:

$$U_m^{3.41} = \overline{U}_{10}^{3.41}, \quad (10)$$

$$U_r^{3.41} = \sum_i w_i U_{10,i}^{3.41}. \quad (11)$$

Sub-grid wind-driven aerosol emissions in CAM5

K. Zhang et al.

[Title Page](#)

[Abstract](#)

[Introduction](#)

[Conclusions](#)

[References](#)

[Tables](#)

[Figures](#)

◀

▶

◀

▶

[Back](#)

[Close](#)

[Full Screen / Esc](#)

[Printer-friendly Version](#)

[Interactive Discussion](#)



Title Page	
Abstract	Introduction
Conclusions	References
Tables	Figures
◀	▶
◀	▶
Back	Close
Full Screen / Esc	
Printer-friendly Version	
Interactive Discussion	

The subscripts “m” (for “mean”) and “r” (for “reference”) denote the quantities calculated without and with the consideration of sub-grid wind variability, respectively. The relative differences diagnosed from the ECMWF data are shown for an arbitrarily chosen time instance in Fig. 3a, and for the annual mean in Fig. 3b. For about 75 % of the ocean grid points, the relative difference is small (less than –10 % in magnitude). On the other hand, local differences exceeding –30 % in magnitude cover about 8 % of the ocean area. The largest spatial variances are mainly associated with precipitation events driven by convective activities.

In Fig. 4, a similar comparison is presented using the WRF simulation over the Southern Ocean. Results are shown for the four 225 km grid boxes located at the center of the WRF domain, presented as time series for the entire simulation period (October 2008). Although the grid spacing of the WRF simulation is a factor of five smaller than that of the ECMWF analysis, the relative differences between $U_m^{3.41}$ and $U_r^{3.41}$ are similar: most of the time, $U_{10}^{3.41}$ calculated from the grid-box mean wind speed agrees within 5 % with the reference result ($U_r^{3.41}$); but there are also events occurring every 3–5 days during which the discrepancies can increase to –30 to –50 %.

To get a rough estimate of the impact of sub-grid wind variability on dust emission, we start from Eq. (5) and assume there is only one PFT in each coarse-resolution grid box. Since the dominant term (in terms of sub-grid variability) in the formula is u_*^3 , and u_* is closely related to the 10 m wind U_{10} , we further simplify the analysis by comparing

$$U_m^3 = \overline{U}_{10}^3, \text{ and} \quad (12)$$

$$U_r^3 = \sum_i w_i U_{10i}^3. \quad (13)$$

(More accurate comparisons of the online CAM5 simulations are presented in Sect. 5.) The errors caused by using the grid-box mean wind speed, diagnosed using the ECMWF analysis and the WRF simulation, are shown in Figs. 5 and 6, respectively. The relative differences are typically between –10 and –50 % in Western China, Central Asia and Western US, which are important dust source regions (Fig. 5). The WRF

simulation in West China contains a strong-wind event around day 4, during which the relative differences between U_m^3 and U_r^3 increase to –20 to –50 %.

The results shown above suggest that considering only the grid-box mean wind speed can lead to substantial inaccuracies on the parameterized aerosol emission, especially for dust. For a more accurate estimate of the impact of surface wind SGV on aerosol emissions and climatology in CAM5, it is worth implementing multiple emission calculations using different wind samples. In the next section, we present and evaluate a method that derives wind speed samples using GCM-predicted mean states.

4 Approximating sub-grid wind variability

Earlier studies have shown that the Weibull distribution is useful and appropriate for representing the temporal frequency distribution of wind speed, for example for wind energy applications (Justus et al., 1978). Ridley et al. (2013) showed that if the sub-grid variance inside a GCM grid box is known, using the Weibull PDF to represent the sub-grid variability of surface wind speed can help improve the accuracy of the emission calculation compared to a simulation that does not account for the SGV. In this section we discuss empirical methods to estimate the sub-grid wind distribution using GCM-predicted physical quantities.

4.1 Weibull distribution

Assuming the wind speed U is a random variable, the probability density function (PDF) of a Weibull distribution can be written as

$$p(U; k, c) = \left(\frac{k}{c}\right) \left(\frac{U}{c}\right)^{k-1} e^{-(U/c)^k} \quad (14)$$

where k is the shape parameter and c the scale parameter. k and c can be derived from the mean (\bar{U}) and the standard deviation (σ_U) using “method 3” of Justus et al.

[Title Page](#)

[Abstract](#)

[Introduction](#)

[Conclusions](#)

[References](#)

[Tables](#)

[Figures](#)

[◀](#)

[▶](#)

[◀](#)

[▶](#)

[Back](#)

[Close](#)

[Full Screen / Esc](#)

[Printer-friendly Version](#)

[Interactive Discussion](#)



$$k = \left(\frac{\bar{U}}{\sigma_U} \right)^{1.086} \quad (15)$$

$$c = \frac{\bar{U}}{\Gamma(1 + 1/k)} \quad (16)$$

where Γ is the Gamma function.

- We note that k and c computed from Eqs. (15) and (16) are approximations which define a new Weibull distribution that features exactly the same mean \bar{U} but differs from the original distribution in terms of higher moments. To evaluate the impact of the parameter estimation error on our study of aerosol emission, we generated a large number of Weibull distributions with the true shape and scale parameters varied in the range (0, 20). Figure 7a shows the relative error of $U_{10}^{3.41}$ and U_{10}^3 corresponding to the estimated Weibull parameters. The reference values were derived from the original Weibull distributions with known (i.e., true) k and c . The relative errors are independent of the scale parameter c , thus only relationships to the shape parameter are presented here. (The relative errors are plotted against the estimated k , rather than the known true value, to allow for straightforward comparison with Fig. 7b. See below.) Figure 7a shows that the relative errors in $U_{10}^{3.41}$ and U_{10}^3 are both small (within 3 %) when the estimated shape parameter is larger than 1. For $k < 1$, Eqs. (15) and (16) give much less accurate results, but this is expected to have negligible impact on our results presented later in this paper, because as Fig. 7b indicates, the shape parameters of 2° grid boxes derived from the ECMWF analysis rarely drop below 1. The two histograms in Fig. 7b were calculated from 6 hourly global data of January and July 2011. The percentages of grid boxes with $k < 1$ were 0.036 % in January and 0.025 % in July.

The usefulness of the Weibull distribution for representing the sub-grid wind variability can be seen in a diagnostic comparison similar to those shown in Figs. 3 and 5.

Sub-grid wind-driven aerosol emissions in CAM5

K. Zhang et al.

[Title Page](#)

[Abstract](#)

[Introduction](#)

[Conclusions](#)

[References](#)

[Tables](#)

[Figures](#)

◀

▶

◀

▶

[Back](#)

[Close](#)

[Full Screen / Esc](#)

[Printer-friendly Version](#)

[Interactive Discussion](#)



Using the 15 km ECMWF data, we derive the grid-box mean and sub-grid standard deviation of the 10 m wind speed (\bar{U}_{10} and $\sigma_{U_{10}}$, respectively) on the 2° coarse mesh, and calculate the shape and scale parameters k and c using Eqs. (15) and (16). The central 99 % of the resulting Weibull PDF is then divided into 100 bins. The discrete

- 5 PDFs are used in Eqs. (11) and (13), with w_i being the frequency of occurrence of bin i .

The errors in $\bar{U}_{10}^{3.41}$ and \bar{U}_{10}^3 caused by using the Weibull distribution instead of the true sub-grid wind distribution (not necessarily Weibull) turn out to be very small (not shown). In terms of both instantaneous values and annual averages, the use of Weibull
10 distribution typically gives errors of less than 2 % over the ocean and less than 5 % over land. These errors are substantially smaller than in the case when only the grid-box mean values are included in the calculation (Figs. 3 and 5 in the previous section). This suggests that with sufficiently accurate estimates of the parameters, the Weibull
15 distribution is a very good approximation of the spatial variability of the near surface wind speed.

Fitting the Weibull distribution as discussed above requires the sub-grid mean and standard deviation of wind speed. Typically, a GCM provides only the grid-box mean wind vector $\bar{\mathbf{v}}$. The magnitude of that mean wind vector, $|\bar{\mathbf{v}}|$, is an underestimate of \bar{U} , while a better approximation can be obtained using the standard deviation σ_U . Obtaining σ_U is thus a key step for fitting the sub-grid wind speed distribution. Considering
20 that the SGV is caused by parameterized physical processes and sub-grid scale features such as complex topography, the ideal sources of information on σ_U would be the corresponding parameterizations. For example, the representation of cold pool in the Unified Convection Scheme (UNICON, Park, 2014) might be used to estimate the SGV
25 caused by mesoscale organized flow associated with deep convection. A high-order turbulence scheme might provide useful predictions of the Raynold's stress to help estimate the wind variability related to turbulence. Since these are not yet available in the standard version of CAM5, we resort to empirical estimates of σ_U as discussed next.

[Title Page](#)[Abstract](#)[Introduction](#)[Conclusions](#)[References](#)[Tables](#)[Figures](#)[Back](#)[Close](#)[Full Screen / Esc](#)[Printer-friendly Version](#)[Interactive Discussion](#)

4.2 Empirical estimate of σ_U

Relatively simple methods have been used in the literature to estimate the parameters needed to determine a Weibull distribution for wind speed. For example, Grini and Zender (2004) and Capps and Zender (2008) used “method 5” of Justus et al. (1978),
5 i.e.,

$$k = C\sqrt{\bar{U}} \quad (17)$$

with C being a constant. In the work of Grini and Zender (2004), C was set to 0.94 to approximate the sub-grid wind variability on land. Their formula effectively estimates σ_U from \bar{U} using

$$10 \quad \sigma_U = 1.059\bar{U}^{0.54}. \quad (18)$$

Some other studies on dust emission used an even simpler method by assuming k is constant over land (e.g. Menut, 2008).

In this work we are interested in global emissions of sea salt and dust. Preliminary investigations indicated that constant k or Eq. (17) with constant C gave reasonable results over certain locations over land but had large regional discrepancies, and both methods were unsatisfactory over the ocean. Below we use a set of empirical formulae to relate σ_U to four types of physical processes: (i) neutral/stable turbulent mixing ($\sigma_{U,t}$),
15 (ii) dry convective eddy ($\sigma_{U,d}$), (iii) moist convective eddy over the ocean ($\sigma_{U,m}$), and (iv) mesoscale flow associated with sub-grid orography over land ($\sigma_{U,l}$). The total sub-grid standard deviation of surface wind speed is defined as
20

$$\sigma_U = \sqrt{\sigma_{U,t}^2 + \sigma_{U,d}^2 + \sigma_{U,m}^2 + \sigma_{U,l}^2}. \quad (19)$$

Among those processes, the first two are associated with spatial scales that can only be resolved by Large Eddy Simulations (LES) or Direct Numerical Simulations (DNS).

[Title Page](#)

[Abstract](#)

[Introduction](#)

[Conclusions](#)

[References](#)

[Tables](#)

[Figures](#)

◀

▶

◀

▶

[Back](#)

[Close](#)

[Full Screen / Esc](#)

[Printer-friendly Version](#)

[Interactive Discussion](#)



Such simulations, and the related observational data, are still very limited in terms of spatial and temporal coverage (e.g., Dipankar, 2015). We do not have sufficient amount of new, high-resolution data to analyze these processes or evaluate parameterizations. We thus choose to use results from earlier studies in the literature.

- 5 Moist convective eddies and orography related mesoscale flows are partially resolved in the ECMWF 15 km analysis. Since the analysis is available for two years (2011 and 2012), we use the first year to derive empirical relationships for estimating $\sigma_{U,m}$ and $\sigma_{U,l}$, then use the second year to evaluate the fitting. The accuracies of the derived relationships are inherently constrained by the resolution of the analysis data.
- 10 The fact that the 15 km resolution is too coarse to resolve neutral/stable turbulence and dry convective eddies is an advantage to us, in that the sub-grid wind variability estimated from the ECMWF analysis do not include the impact of neutral/stable turbulence and dry convective eddies. There is hence no double-counting between $\sigma_{U,m}$ and $\sigma_{U,l}$ derived from the 15 km analysis, and the $\sigma_{U,t}$ and $\sigma_{U,d}$ estimated using process-based formulation. One might still raise the concern that the 15 km resolution is also 15 too coarse to fully resolve moist convection and fine-scale topography effect. Although the concern is legitimate, we show in the section that the derived relationships are able to give quite accurate emission estimates when evaluated against the WRF simulations (3 km resolution). This provides good confidence in the empirically fitted relationships,
- 20 at least for important regions of sea salt and dust emission that are of interest for our purposes. In the future, it will be useful to further evaluate and update the sub-grid wind variability parameterizations using additional high-resolution data (when they become available). Another useful and challenging research topic is to construct process-based parameterizations instead of empirical fitting as discussed here.

Sub-grid wind-driven aerosol emissions in CAM5

K. Zhang et al.

[Title Page](#)

[Abstract](#)

[Introduction](#)

[Conclusions](#)

[References](#)

[Tables](#)

[Figures](#)

[◀](#)

[▶](#)

[◀](#)

[▶](#)

[Back](#)

[Close](#)

[Full Screen / Esc](#)

[Printer-friendly Version](#)

[Interactive Discussion](#)



4.2.1 Neutral/stable turbulent mixing

To consider the influence of turbulent mixing in a neutral or stable boundary layer, we follow ECMWF (2004) and estimate the resulting wind variability using

$$\sigma_{U,t} = \begin{cases} 2.29 u_* (|\bar{v}|) & \text{when } F_{\theta_v} \leq 0 \\ 0 & \text{when } F_{\theta_v} > 0. \end{cases} \quad (20)$$

- 5 Here F_{θ_v} is the surface buoyancy flux (unit: $\text{m}^2 \text{s}^{-1}$) defined in Zeng et al. (2002), θ_v is the virtual potential temperature (unit: K), $u_* (|\bar{v}|)$ is the friction velocity diagnosed from the speed of the grid-box mean wind $|\bar{v}|$. In Eq. (20) the strength of turbulence is represented by the friction velocity u_* , not the turbulent kinetic energy (TKE, cf., e.g. Cakmur et al., 2004). This choice results from the experience that TKE is not provided by all GCMs, and, when available, its characteristic value and spatio-temporal distribution can differ substantially from model to model.
- 10

4.2.2 Dry convective eddies

The contribution of dry convective eddies to sub-grid wind variability is estimated using a formulation recommended by Redelsperger et al. (2000) and Lunt and Valdes (2002):

$$15 \quad \sigma_d = \begin{cases} 0 & \text{when } F_{\theta_v} \leq 0 \\ \left(\frac{gH\theta_v}{\theta_v} \right)^{\frac{1}{3}} & \text{when } F_{\theta_v} > 0, \end{cases} \quad (21)$$

H is the boundary layer height (unit: m), and g is gravity.

Note that by using the surface buoyancy flux F_{θ_v} as a criterion, we consider contributions from either neutral/stable turbulence mixing (Eq. 20) or dry convective eddies (Eq. 21), but not both, for the purpose of avoiding double-counting.

[Title Page](#)

[Abstract](#)

[Introduction](#)

[Conclusions](#)

[References](#)

[Tables](#)

[Figures](#)

[◀](#)

[▶](#)

[◀](#)

[▶](#)

[Back](#)

[Close](#)

[Full Screen / Esc](#)

[Printer-friendly Version](#)

[Interactive Discussion](#)



4.2.3 Moist convective eddies over the ocean ($\sigma_{U,m}$)

For the influence of moist convective eddies and downdrafts, Redelsperger et al. (2000) constructed an empirical formula based on two 2-D cloud-resolving model (CRM) simulations that covered one week in time and 512 km across the horizontal domain, with a horizontal resolution of 2 km. Their formula uses the surface precipitation rate P (mm day⁻¹) as the predictor for sub-grid wind variability:

$$\sigma_{U,m} = \ln(1 + 6.69 P - 0.47 P^2). \quad (22)$$

In this study we are interested in sea salt emissions, the main sources of which are located in the storm tracks (i.e., mid-latitudes). Given that the Redelsperger et al. (2000) equation was derived from simulations of tropical deep convection with very limited temporal and spatial coverage, it was unclear whether the same relationship would be appropriate for our purpose. We attempted to derive a similar relationship using the ECMWF 15 km analysis of 2011, and indeed found it difficult to obtain one good formula for all latitudes. The best-fit formula for a 2° × 2° GCM grid has the form

$$\sigma_{U,m} = \begin{cases} 0.95 \ln(1 + 4.01 \sqrt{P} + 0.31 P^2) & (\text{ocean}) \\ 0 & (\text{land}) \end{cases} \quad (23)$$

where

$$P = \begin{cases} P_{\text{strat+conv}} & \text{where SST} < 295 \text{ K}, \\ 0.2 P_{\text{strat+conv}} & \text{where SST} \geq 295 \text{ K}. \end{cases} \quad (24)$$

The SST criterion essentially distinguishes the tropics and mid-latitudes.

Figure 8 presents time series of the sub-grid standard deviation of surface wind speed calculated with Eqs. (22) and (23), and the values directly derived from the ECMWF analysis. The results are shown for January 2012 for a few arbitrarily chosen 10° × 10° regions (cf. Fig. 1). Results in other months are similar and thus not shown. In

the low latitudes, the Redelsperger et al. (2000) formula predicts considerably higher wind variability than both our fitting and the ECMWF analysis. This is consistent with expectation since the CRM simulations which the Redelsperger et al. (2000) is based on are capable of resolving substantially more convective activity than the ECMWF analysis.

5 In the middle latitudes, however, the two formulae give very similar estimates, and both agree reasonably well with the ECMWF analysis.

Given the 15 km resolution, one might still question whether the ECMWF analysis is an appropriate reference for the evaluation here. To address this issue, Fig. 9 evaluates the two empirical formulae by comparing the estimates with the WRF simulation over

10 the Southern Ocean. For each of the $225 \text{ km} \times 225 \text{ km}$ box at the center of the WRF domain, the diagnosed sub-grid variability is shown in black and the estimated values in red and blue. Again, the two empirical formulae give very similar results. Both are able to capture the mean wind variability over the simulated period, and the most frequently occurring high and low values, although the strongest peaks are underestimated. The

15 Redelsperger et al. (2000) formula gives larger peak values than our fitting derived from the ECMWF data, but the differences are relatively small. On the whole, the two empirical formulae have similar predicting skills; This provides confidence that they are both suitable for estimating sub-grid wind variability in mid-latitudes. In principle one could also conduct and analyze a high-resolution WRF simulation of deep convection

20 to get more insight into the discrepancies in the tropics between our fitting and the Redelsperger et al. (2000) formula (Fig. 8). However, since the tropics have relatively small contribution to the global sea salt emission, we have not included such a WRF simulation in this paper.

4.2.4 Mesoscale flows over land ($\sigma_{U,l}$)

25 The sub-grid wind speed variance diagnosed from the ECMWF analysis (Fig. 2 in Sect. 3) indicates clearly that over land, the strongest variabilities are associated with complex topography. Such disturbances can be caused by pure dynamical effects, but they can also involve moist processes (e.g. cumulus convection), and thus are difficult

Title Page	
Abstract	Introduction
Conclusions	References
Tables	Figures
◀	▶
◀	▶
Back	Close
Full Screen / Esc	
Printer-friendly Version	
Interactive Discussion	



to parameterize. A preliminary investigation showed that for individual locations, the sub-grid wind variance is strongly correlated with the grid-box mean wind speed. We therefore follow the idea of Eq. (17) but, unlike earlier studies in the literature, make C a location dependent and time-invariant parameter, i.e.,

$$k(x, y, t) = C(x, y) \sqrt{\bar{U}(x, y, t)} \quad (25)$$

where x and y denote longitude and latitude, respectively. The parameter C is derived from the ECMWF analysis using the following procedure: first, for each 2° grid cell, calculate the grid-box mean wind speed and the sub-grid standard deviation; second, calculate k using Eq. (15); third, derive the time-invariant C using temporally averaged \bar{U} and k , i.e.,

$$C(x, y) = \frac{\sum_{t=1}^n k(x, y, t)}{\sum_{t=1}^n \sqrt{\bar{U}(x, y, t)}}. \quad (26)$$

The time index t goes through all 6 hourly samples of the year 2011. After determining C , the standard deviation of sub-grid wind speed is calculated by

$$\sigma_{U,I} = \begin{cases} 0 & \text{(ocean)} \\ \left(\frac{\bar{U}}{C}\right)^{0.586} & \text{(land)} \end{cases}^{1/1.086} \quad (27)$$

In Fig. 10, the coefficient C derived from the 2011 ECMWF analysis is shown in potential dust source regions. The spatial pattern of C is strongly correlated with topography. As a result, C shows substantial regional variation: the typical values are below 2 in Asia and South America, but above 3 in Australia and North Africa. Within these

Sub-grid wind-driven aerosol emissions in CAM5

K. Zhang et al.

[Title Page](#)

[Abstract](#)

[Introduction](#)

[Conclusions](#)

[References](#)

[Tables](#)

[Figures](#)

[◀](#)

[▶](#)

[◀](#)

[▶](#)

[Back](#)

[Close](#)

[Full Screen / Esc](#)

[Printer-friendly Version](#)

[Interactive Discussion](#)



regions, the coefficient also has substantial spatial variation at the thousand-kilometer scale.

Since the coefficient C is inversely correlated with the sub-grid wind speed variance (Eq. 27), using a global constant can lead to large regional biases. This is confirmed by Fig. 11 which evaluates surface wind SGV estimated by Eqs. (26) and (27) with both spatially varying and fixed C against SGV derived from the ECMWF data. In the case of fixed C , the constant value of 0.94 comes from method 4 of Justus et al. (1978), and has been used by Grini and Zender (2004) and Capps and Zender (2008). Time series of the sub-grid standard deviation of surface wind speed in January 2012 are shown for ten 2° grid boxes in North Africa (Fig. 11a–c), East Asia (Fig. 11d–f), Australia (Fig. 11g and h), and North America (Fig. 11i–h). The empirical formula with spatially variant C (blue lines in Fig. 11) is able to capture the characteristic magnitude of the wind variability, as well as main features of the temporal evolution. In contrast, the wind variability estimated with $C = 0.94$ is about 100–200 % larger than the analysis in Australia, and more than a factor of 3 stronger in Northwest Africa, where the topography is relatively flat.

It is also worth noting that for our empirical estimates shown in Fig. 11, the coefficient C is derived from the analysis of 2011 but applied to the year 2012. The agreement between the empirical estimate and the analysis suggests that the relationship between grid-box mean wind speed and sub-grid wind variance is not strongly affected by interannual variability of the general circulation.

In Fig. 12, estimates of sub-grid wind speed variability based on constant and locally fitted C are evaluated using the 7 day WRF simulation near the Taklamakan Desert. The black curves in the figure indicate wind variability in the four $225 \text{ km} \times 225 \text{ km}$ boxes at the center of the WRF domain (cf. Fig. 1), derived from the 3 km model output. The red curves are the estimates based on $C = 0.94$. The results shown in blue are calculated using the C values fitted from the ECMWF analysis for the $2^\circ \text{ lat} \times 2^\circ \text{ lon}$ grid cells that are closest to the 225 km boxes. Although the ECMWF analysis does not resolve scales smaller than 15 km, the coefficient C derived from the ECMWF data leads to

[Title Page](#)[Abstract](#)[Introduction](#)[Conclusions](#)[References](#)[Tables](#)[Figures](#)[◀](#)[▶](#)[◀](#)[▶](#)[Back](#)[Close](#)[Full Screen / Esc](#)[Printer-friendly Version](#)[Interactive Discussion](#)

Sub-grid wind-driven aerosol emissions in CAM5

K. Zhang et al.

[Title Page](#)

[Abstract](#)

[Introduction](#)

[Conclusions](#)

[References](#)

[Tables](#)

[Figures](#)

◀

▶

◀

▶

[Back](#)

[Close](#)

[Full Screen / Esc](#)

[Printer-friendly Version](#)

[Interactive Discussion](#)



very reasonable estimates of wind variability compared to the 3 km WRF simulation. Estimates made with $C = 0.94$ also agree reasonably with the WRF simulation, and are similar to results obtained with location-dependent C . This is consistent with the fact that our fitted C values are in the range of 1.19 to 1.56 in the four 225 km boxes, which are not substantially from the value 0.94.

It is worth noting again that the coefficient C fitted from the ECMWF analysis have values close to 1 in regions of complex topography (e.g., Western China), and considerably larger values in regions where the surface is relatively flat (e.g., Australia and western part of North Africa, see Fig. 10). The evaluation against the WRF simulation in Western China (Fig. 12) provides confidence in the ECMWF analysis and the fitted C values in regions of fine-scale topographical features. Since the 15 km analysis should have less resolution problem with relatively flat and homogeneous topography, one can thus expect the fitted C values to be more accurate in those regions. It follows that using globally uniform $C = 0.94$ would probably cause considerable overestimates of sub-grid wind variability in Australia, North Africa, and Arabia.

4.3 Implementation in CAM5

In the previous subsections we have shown that the Eqs. (23) and (24) and (26) and (27) can provide very good estimates of the sub-grid wind speed variability when compared with the ECMWF analysis and WRF simulations. These empirical relationships are combined with Eqs. (20) and (21) to provide an estimate of the total sub-grid variance of surface wind speed σ_U using Eq. (19).

Given the GCM predicted grid-box mean wind vector $\bar{\mathbf{v}}$ and the estimated σ_U , we assume that the sub-grid mean wind speed can be approximated by

$$\bar{U} \approx \sqrt{|\bar{\mathbf{v}}|^2 + \sigma_U^2}. \quad (28)$$

This is similar to Eq. (7) which originated from Zeng et al. (2002), but takes into account additional sources of wind speed SGV.

\bar{U} and σ_U are used in Eqs. (14)–(16) to determine a Weibull distribution. Surface wind speed samples U_j are obtained by equally divide the central 99 % of the Weibull PDF in to 100 bins. Sensitivity simulations with a 20 bin Weibull PDF show similar results. From the surface wind speed samples, the corresponding values of 10 m wind speed and friction velocity are derived, and used to calculate the grid-box mean sea salt and dust emission fluxes following Sect. 2.5. If the estimated σ_U is smaller than 0.1 ms^{-1} , we skip the derivation of Weibull PDF and wind samples, and use only the mean wind speed for the emission calculations. The computation cost for the sub-grid treatment is small (less than 3 % of the total simulation cost).

The next section presents a series of CAM5 simulations to quantify the impact of sub-grid wind variability on aerosol emission and the model's mean climate. For clarification, we note that the σ_U and \bar{U} (Eq. 28) described above are applied only to the sea salt and dust emission parameterizations. As mentioned at the end of Sect. 2.4, the default model uses an adjusted mean wind speed (Eq. 7) for all calculations related to surface fluxes and boundary layer processes over land. This is unchanged in our simulations except for dust emission. We chose not to modify Eq. (7) so as to cleanly separate the impact of sub-grid variability on aerosol emission from the impacts on other physical processes.

5 Impact on aerosol climatology in CAM5

CAM5 simulations have been conducted for the year 2006. Each simulation includes a 3 month spin-up (October–December 2005) which is not included in the analysis in this section. The horizontal winds were nudged to the ERA-Interim reanalysis with a relaxation time scale of 6 h. Temperature and humidity were not nudged, since earlier experiences have shown that directly constraining these two fields might lead to substantially different model climate (Zhang et al., 2014; Jeuken et al., 1996). Details of the nudging implementation are described in Zhang et al. (2014). Nudging effectively

Title Page	Abstract	Introduction
Conclusions	References	
Tables	Figures	
◀	▶	
◀	▶	
Back	Close	
Full Screen / Esc		
Printer-friendly Version		
Interactive Discussion		



constrains the large-scale circulation and suppresses the noise caused by natural variability, thus allowing for detection of changes in the simulated aerosol characteristics and their climate effects using substantially shorter simulations (see, e.g., Kooperman et al., 2012).

5 The control simulation and sensitivity experiments are summarized in Table 1. Experiment CTRL uses the default configuration of CAM5, in which the impact of dry convective eddies is taken into account when estimating the grid-box mean wind speed \bar{U}_{adj} (Eq. 7). \bar{U}_{adj} is used for calculating dust emission, while the parameterization of sea salt emission does not account for sub-grid wind variability (Eq. 2). Simulation EXP1
10 is similar to CTRL in that only dry convective eddies are considered for the wind SGV. The differences are that (i) the dust emissions are calculated using the wind speed PDF (Eq. 9), and (ii) the same PDF-based method is also applied to sea salt emission (Eq. 8). EXP2 extends EXP1 by adding the contribution of turbulence in neutral and stable boundary layers, and EXP3 further extends EXP2 by including the impact
15 of moist convective eddies over the ocean and topography related small-scale motions over land. For completeness, we also conducted a simulation called NOSG, in which the dust emission is calculated using the speed of grid-box mean wind, $|\bar{v}|$, instead of \bar{U}_{adj} ; in other words, NOSG does not include any effect of sub-grid wind variability on dust emission. The simulations NOSG, CTRL, EXP1, EXP2 and EXP3 are analyzed
20 in Sect. 5.1 to quantify the contribution of different source of wind variability to the emission and concentration of sea salt and dust aerosols.

As is shown later in Sect. 5.1, EXP3 features considerably stronger dust emission and higher dust AOD (Aerosol Optical Depth). In global aerosol-climate models, it is a common practice to apply a constant scaling factor to the dust emission, for the
25 purpose of adjusting the global mean dust AOD as well as the aerosol induced radiative forcing. The default scaling factor in CAM5 for the 2° finite-volume dynamical core is 0.35^{-1} (here we follow the form of the scaling factor defined in the model). This value is used in NOSG, CTRL, EXP1, EXP2 and EXP3. When discussing the aerosol climatology and radiative forcing in Sect. 5.2, we also present an additional simulation,

Sub-grid wind-driven aerosol emissions in CAM5

K. Zhang et al.

[Title Page](#)

[Abstract](#)

[Introduction](#)

[Conclusions](#)

[References](#)

[Tables](#)

[Figures](#)

◀

▶

◀

▶

[Back](#)

[Close](#)

[Full Screen / Esc](#)

[Printer-friendly Version](#)

[Interactive Discussion](#)



EXP4, which used the same configuration as EXP3, but the dust emission factor is adjusted to 0.57^{-1} which brings the global and annual mean dust emission flux back to the value of the CTRL simulation.

5.1 Contribution of individual sources of wind variability

- 5 Figure 13 depicts geographical distributions of the annual mean sea salt emission and
sea salt AOD (Aerosol Optical Depth) in the various simulations, and Table 2 compares
the globally or regionally averaged emission fluxes. In the default model (Fig. 13a and
b), the strongest sea salt emission occurs in the mid-latitude storm tracks where the
majority of the released particles are subsequently removed by precipitation. The trade
10 wind regions have moderate emission but very weak wet removal, which leads to high
sea salt concentrations. In the deep tropics, the default model predicts very low emis-
sion because the impact of frequent and vigorous convective activity on surface wind
SGV is not considered, and the grid-box mean wind speed is low. The low emission, in
combination with strong removal associated with the parameterized convection, results
15 in low sea salt AOD in regions of strongest convective precipitation.

The impacts of sub-grid wind variability on sea salt emission and optical depth are generally small and spatially homogenous except in the Inter Tropical Convergence Zone (ITCZ). The dry convective eddies lead to negligible (< 1 %) increase in both the emission and the AOD at most of the ocean grid boxes (Fig. 13c and d, and EXP1-CTRL in Table 2); including the impact of neutral and stable turbulence ($\sigma_{U,t}$) increases emission flux by 2–5 % (Fig. 13e and f, and EXP2-EXP1 in Table 2); including moist convective eddies further enhances the impacts to about 5–10 % outside the ITCZ (Fig. 13g and h, and EXP3-EXP2 in Table 2). Within the ITCZ, the sub-grid wind variability estimated using our empirical relationship results in 10–35 % increases (compare to the default model) in the annual mean sea salt emission and 10–25 % increases in sea salt AOD. If we had chosen to use the formula of Redelsperger et al. (2000) for the moist convective eddies, the impacts would be even stronger. However, since the baseline values of emission fluxes are low in the ITCZ and the wet removal



is strong, the contribution of these regions to the global total sea salt budget is small. In terms of global and annual average, the increase in sea salt emission is about 7% (Table 2) when comparing out EXP3 to CTRL. This number is not expected to change considerably if the formula of Redelsperger et al. (2000) is applied.

5 The simulated dust emission and optical depth are more sensitive to sub-grid wind variability than sea salt. This can be seen in Fig. 14 which shows the geographical distributions of the annual mean dust emission and AOD in the various simulations, and in Table 3 which compares dust emissions in the major source regions. In both the control simulation and EXP1, dry convective eddies are taken into account when
10 estimating the grid-box mean wind speed for dust emission; however, using multiple wind samples instead of the mean value leads to about 30 % emission increases in Asia and North Africa, and even larger differences in North America and South America (Fig. 14c and d, and EXP1 in Table 3). This reflects the strong nonlinearity of the dust emission parameterization. Part of the nonlinearity comes from the fact that the
15 parameterization requires the characteristic friction velocity u_{*s_j} to exceed the threshold value u_{*t} in order for dust emission to occur (cf. Eq. 5).

The neutral/stable turbulence has relatively small impact, which is consistent with Cakmur et al. (2004). They cause about a 3 % increase in the global mean dust emission, and similar increases in Asia, North Africa, and North and South America. The
20 related AOD changes are hardly discernible (Fig. 14f vs. d). In contrast, considering the small-scale motions related to sub-grid topography results in a 23 % increase of the annual mean global dust emission (comparing EXP3 with EXP2 in Table 3). The regional enhancements are about 13 % in North Africa, and about 40 % in East Asia. The increases in AOD are evident in these source regions and the downwind areas
25 (Fig. 14h vs. f). In Table 3 we also included the emission fluxes from the NOSG simulation. Combined with EXP1, these numbers quantify the total impact of dry convective eddies. From the table, it is clear that dry convective eddies and meso-scale flows associated with sub-grid scale topography are the most important factors that affect dust emission in CAM5.

Sub-grid wind-driven aerosol emissions in CAM5

K. Zhang et al.

[Title Page](#)[Abstract](#)[Introduction](#)[Conclusions](#)[References](#)[Tables](#)[Figures](#)[◀](#)[▶](#)[◀](#)[▶](#)[Back](#)[Close](#)[Full Screen / Esc](#)[Printer-friendly Version](#)[Interactive Discussion](#)

5.2 Total AOD and radiative forcing

The diagnostics above showed that applying the PDF method to take into account sub-grid wind speed variability leads to considerable increases in the emission and loading of dust aerosols. To evaluate how much the increases affect the agreement and discrepancies between model simulation and observation, the simulated annual mean total AOD is compared against the satellite retrieval obtained with the Multi-angle Imaging SpectroRadiometer (MISR) in 14 major dust source regions (Fig. 15). The definition and indexing of the 14 regions follow Zender and Kwon (2005). Model data are sampled at the satellite local overpass time (13:30), and are masked out when the corresponding MISR record indicates missing data. Note that we modified the model source code to calculate the aerosol optical properties at each model time step, rather than doing the calculation when the radiation calculation is called every two hours as in the standard model. The comparison indicates that, except in regions 3, 8 and 5 (North America and South Africa), the total AOD in EXP3 is higher than that of CTRL by 14–71 %, and higher than the MISR data by 6–167 % (Fig. 15). The largest differences are found in regions 2 and 9 (North Africa), 7 and 13 (China), and 10–12 (Arabia), all of which correspond to relatively small values of the coefficient C in Fig. 10 which reflect the impact of complex sub-grid scale topography. By changing the dust emission scale factor from 0.35^{-1} to 0.57^{-1} , the global mean emission flux is brought back to the value in CTRL with a less than 5 % difference. Subsequently, the regional AOD values also become similar to those in CTRL (Fig. 15).

In Fig. 16, the aerosol-induced radiative forcings are presented as annually averaged top-of-atmosphere (TOA) flux differences between EXP3 and CTRL. The clear-sky shortwave flux differences (Fig. 16a) generally exceed 2 W m^{-2} in the dust source regions in North Africa, Arabia, and Western China, due to the absorption of solar radiation by dust aerosols. In the downwind areas of those regions, negative values of -0.5 to -5 W m^{-2} show that after mixing with hygroscopic species, the enhanced dust

Sub-grid wind-driven aerosol emissions in CAM5

K. Zhang et al.

[Title Page](#)

[Abstract](#)

[Introduction](#)

[Conclusions](#)

[References](#)

[Tables](#)

[Figures](#)

◀

▶

◀

▶

[Back](#)

[Close](#)

[Full Screen / Esc](#)

[Printer-friendly Version](#)

[Interactive Discussion](#)



concentration results in stronger scattering of solar radiation. The impact of sea salt emissions changes is much smaller ($< 0.5 \text{ W m}^{-2}$).

In terms of the longwave radiation, the clear-sky flux differences (Fig. 16b) are positive both in the dust source regions and in the immediate neighborhood, due to the strong absorption of longwave radiation by coarse mode dust aerosols (Stier et al., 2007). The typical clear-sky flux differences are $1\text{--}5 \text{ W m}^{-2}$ locally. The positive all-sky flux differences (Fig. 16c) in North Africa, Arabia and middle latitude regions of Asia are about twice as large as the clear-sky differences, suggesting that the stronger dust emissions have also led to enhanced formation of ice clouds. Since those are largely arid regions, there is limited water vapor transport to the upper troposphere either by horizontal advection or by convective transport. Ice crystal formation in these regions is thus dominated by heterogeneous ice nucleation, and the concentration of dust aerosols is a major factor affecting the ice nucleation rate.

Over the low-latitude ocean and in South America, the all-sky longwave flux differences seen in Fig. 16c are mostly noise related to tropical convection, since the wind-only nudging does not strongly constrain the thermodynamic state of the atmosphere under weak Coriolis force. On the other hand, over the western part of the marinetime continent and between $0\text{--}30^\circ \text{ S}$ in South America, there are regions associated with substantially decreased absorption of longwave radiation.

In those regions, strong convective transport of water vapor often produces high ice supersaturation ($\text{RH}_i > 150\%$) in the upper troposphere and frequent homogeneous ice nucleation in the CTRL simulation. The stronger dust emission and higher dust aerosol concentrations in EXP3 facilitates more frequent heterogeneous ice nucleation. This efficiently reduces the relative humidity and inhibits homogeneous ice nucleation (Liu et al., 2012b; Zhang et al., 2013). The net effect is reduced ice cloud fraction, weaker absorption of longwave radiation, and weaker warming.

When the global mean dust emission is adjusted back to the CTRL level in EXP4, the TOA clear-sky flux differences become negligible, and the TOA all-sky flux differences mainly show the noise related to tropical convection (not shown). However, the lack

Sub-grid wind-driven aerosol emissions in CAM5

K. Zhang et al.

[Title Page](#)

[Abstract](#)

[Introduction](#)

[Conclusions](#)

[References](#)

[Tables](#)

[Figures](#)

◀

▶

◀

▶

[Back](#)

[Close](#)

[Full Screen / Esc](#)

[Printer-friendly Version](#)

[Interactive Discussion](#)



Sub-grid wind-driven aerosol emissions in CAM5

K. Zhang et al.

[Title Page](#)[Abstract](#)[Introduction](#)[Conclusions](#)[References](#)[Tables](#)[Figures](#)[|◀](#)[▶|](#)[◀](#)[▶](#)[Back](#)[Close](#)[Full Screen / Esc](#)[Printer-friendly Version](#)[Interactive Discussion](#)

of physically significant differences between EXP4 and CTRL in terms of the annual mean TOA fluxes (not shown) and regional mean AOD (Fig. 15) does not mean the impact of sub-grid wind variability is nullified. In the upper row of Fig. 17, frequency distributions of the simulated dust emission fluxes are shown for three grid points in

5 the Taklamakan Desert (western China), the Bodele Depression (north central Africa), and East Australia, respectively. The distributions were derived from hourly emission fluxes for the whole year (2006). In the Taklamakan Desert and the Bodele Depression (Fig. 17), the introduction of sub-grid wind variability without tuning the global mean dust emission leads to more frequent dust emission at all emission levels except for

10 the leftmost flux bin in each panel which includes zero flux. Re-tuning the emission results in less frequent occurrence of stronger emissions, and more frequent occurrence of weaker emissions. Because the re-tuning is implemented globally using a constant scaling factor, the same qualitative change is seen also in regions where the sub-grid wind variability is relatively small (e.g., Australia, Fig. 17c). The lower row of Fig. 17

15 shows the relative contribution of each flux range to the total dust emission in the three locations, again derived from hourly data for 2006. The three panels further confirm that after the re-tuning, EXP4 features smaller contributions from stronger emission events, and larger contributions from weaker emission events. Since these fluxes are grid-box averages in a 2° model grid, the shift of emission distribution seems physically

20 plausible, although there is not yet a good observational dataset to evaluate whether such a shift also makes the simulated emissions more realistic. Satellite retrievals are severely limited by the sampling frequency (one overpass per day), while the Aeronet data are pointwise measurements, and comparing them with regional averages is not straightforward. The shift in emission flux distribution also has implication on the instantaneous aerosol forcing as well as its impact on local circulation.

5.3 Comments on resolution sensitivity

It is a common feature of many global aerosol-climate models (including CAM5) that the simulated surface wind speeds and aerosol emissions are sensitive to model reso-

Sub-grid wind-driven aerosol emissions in CAM5

K. Zhang et al.

lution (e.g. Gläser et al., 2012). This is in fact the reason why the dust emission factor in Table 1 was introduced in the first place; and this parameter is often adjusted in simulations at different resolutions for the purpose of achieving the desired energy balance. Now that an empirical method has been developed in this study to account for the impact of sub-grid wind variability, a natural question to ask is whether this PDF-based method makes the dust emission parameterization scale-aware, and hence reduces the resolution sensitivity of the simulated dust emission. To answer this question, we first note that in this study, the sub-grid wind speed PDF is determined by the grid-box mean and standard deviation of the surface wind speed (\bar{U} and σ_U), which in turn depends on

- (i) the GCM resolved grid-box mean surface wind \bar{v} , and
- (ii) the various components of the sub-grid wind variability, namely $\sigma_{U,t}$, $\sigma_{U,d}$, $\sigma_{U,m}$, and $\sigma_{U,l}$.

This study made an attempt to address the second aspect for a GCM resolution of $2^\circ \text{lat} \times 2^\circ \text{lon}$. For other resolutions, the coefficient C used for estimating the topography related wind variability (Eq. 27) needs to be re-derived using Eq. (26). (Similarly, for aerosol emissions over the ocean, the coefficients in Eqs. (23) and (24) also need to be re-derived for different resolutions.) In addition to σ_U , the grid-box mean wind \bar{v} also determines the sub-grid wind speed distribution, and \bar{v} is mainly affected by the large-scale dynamics, convection parameterization, and surface properties. These aspects of an atmospheric GCM are out of the scope of the current work. The resolution sensitivity of dust emission can be removed when all model components are scale-aware. Since only part of the necessary conditions are addressed in this study, we do not expect the dust emissions simulated at different resolutions to agree with each other.

Title Page	
Abstract	Introduction
Conclusions	References
Tables	Figures
◀	▶
◀	▶
Back	Close
Full Screen / Esc	
Printer-friendly Version	
Interactive Discussion	



6 Conclusions

In this paper we evaluated the impact of sub-grid surface wind variability on sea salt and dust emissions in CAM5. The basic strategy is to calculate emission fluxes multiple times in each GCM grid cell, using different samples of a wind speed distribution derived from model-predicted grid-box mean quantities.

Simplified diagnostic calculations were conducted first, using year 2011 of the ECMWF operational analysis (15 km resolution), and two simulations with the WRF model at 3 km resolution, one for a 900 km × 900 km domain over the Southern Ocean, and the other with the same domain size but located in Western China near the Taklamakan Desert. The high-resolution meteorological data was regridded to coarse resolution grids (2° lat × 2° lon for ECMWF and 225 km resolution for WRF), and sea salt and dust emissions were calculated using both high and coarse resolution surface wind speeds then compared.

Sea salt emissions calculated using the coarse resolution grid-box mean wind speed were reasonably accurate (with less than a few percent error) in terms of annual mean, but instantaneous emission fluxes were more severely underestimated at times. For dust emissions, non-negligible errors were seen both in instantaneous emissions and in annual averages, suggesting that the impact of sub-grid wind variability needs to be taken into account. It was also confirmed that when the mean and standard deviation of surface wind speed are known accurately, the Weibull distribution provides a good characterization of the probability distribution of the sub-grid wind speed, from which different samples can be drawn for the emission calculation.

In order to estimate the sub-grid wind speed distribution in the CAM5 global climate model using the available model-predicted physical quantities, we developed a method to approximate the sub-grid standard deviation of surface wind speed using four components. The contributions of neutral/stable turbulence and dry convective eddies were estimated using parameterizations from previous studies. The wind variabilities caused by moist convective eddy over the ocean and small-scale topography over land were

Sub-grid wind-driven aerosol emissions in CAM5

K. Zhang et al.

[Title Page](#)

[Abstract](#)

[Introduction](#)

[Conclusions](#)

[References](#)

[Tables](#)

[Figures](#)

◀

▶

◀

▶

[Back](#)

[Close](#)

[Full Screen / Esc](#)

[Printer-friendly Version](#)

[Interactive Discussion](#)



Title Page	
Abstract	Introduction
Conclusions	References
Tables	Figures
◀	▶
◀	▶
Back	Close
Full Screen / Esc	
Printer-friendly Version	
Interactive Discussion	



estimated using empirical relationships derived from the 15 km ECMWF analysis of 2011. Evaluation against the year 2012 analysis of ECMWF showed that the empirical relationships can capture the sub-grid variability of surface wind speeds reasonably well. Further evaluation using the 3 km WRF simulations suggested that the formulae derived using the ECMWF analysis are not severely limited by the 15 km horizontal resolution.

The online calculated sub-grid wind speed distributions were used in the sea salt and dust emission parameterizations in CAM5 simulations of the year 2006 at 2° horizontal resolution with 30 vertical levels. The CAM5 simulations confirm conclusions from the simplified diagnostic calculation that sub-grid wind variability has relatively small impacts on the annual mean emission of sea salt aerosols, but considerable influence on the emission of dust. Among the considered mechanisms, dry convective eddies and small-scale topography are the major causes of dust emission increases when sub-grid wind variability is taken into account. With all the four components included and no additional adjustment of uncertain parameters in the model, the simulated global and annual mean dust emission increase by about 50 % compared to the default model. The dust AOD in the source regions in Central and Eastern Asia increases by more than 100 %, while that in North Africa, Arabia, and the downwind regions in East Asia increases between 50 and 100 %. The increased dust loading results in stronger absorption of longwave radiation by $1\text{--}5 \text{ W m}^{-2}$ or higher in the low- and middle-latitude regions in Africa and Asia, both through direct absorption by dust, and because of the increased ice cloud fraction. In the tropical regions where moist convection is active, higher dust concentrations in the upper troposphere enhances heterogeneous ice nucleation and inhibits homogenous ice nucleation, giving a net effect of weaker longwave absorption.

When sub-grid wind variability is taken into account, the total AOD simulated in dust source regions is considerably higher than both the default model and the MISR retrieval. By tuning the globally constant dust emission scale factor, the dust emission, AOD, and top-of-atmosphere radiative fluxes can be adjusted to the level of the default

model, but the frequency distribution of dust emission changes, with more contribution from weaker events and less contribution from stronger events. This shift seems reasonable for 2° grid cells, but whether it is more realistic is not yet clear due to the lack of observational data for validation.

5 Code availability

The CESM version 1.2.0 release can be obtained at (<http://www.cesm.ucar.edu/models/cesm1.2/>). Code modifications for the sub-grid treatment of wind-driven aerosol emission calculations are available upon request by contacting the corresponding author.

- 10 *Acknowledgements.* This work was supported by the U.S. Department of Energy (DOE) office of Science as part of the Scientific Discovery Through Advanced Computing (SciDAC) project on Multiscale Methods for Accurate, Efficient, and Scale-Aware Models of the Earth System. The Pacific Northwest National Laboratory is operated for DOE by Battelle Memorial Institute under contract DE-AC06-76RLO 1830. We thank Charlie Zender for making the
- 15 Dust Entrainment and Deposition Model (DEAD) available for public access. We are also grateful to Phil Rasch and Po-Lun Ma (PNNL) for helpful discussions. Computational resources (ark:/85065/d7wd3xhc) at the NCAR-Wyoming Supercomputing Center were provided by the National Science Foundation and the State of Wyoming, and supported by NCAR's Computational and Information Systems Laboratory. Computational resources at the Pacific Northwest
- 20 National Laboratory were provided by the PNNL Institutional Computing (PIC). The ECMWF operational analysis used in this study were obtained from the Research Data Archive (RDA) maintained by the Computational and Information Systems Laboratory (CISL) at the National Center for Atmospheric Research (NCAR). NCAR is sponsored by the National Science Foundation (NSF). Post-processing was done using the Climate Data Operators (CDO, available at: <http://www.mpimet.mpg.de/cdo>) and the NCAR Command Language (NCL, available at: <http://dx.doi.org/10.5065/D6WD3XH5>).

GMDD

8, 7249–7312, 2015

Sub-grid wind-driven aerosol emissions in CAM5

K. Zhang et al.

Title Page	
Abstract	Introduction
Conclusions	References
Tables	Figures
◀	▶
◀	▶
Back	Close
Full Screen / Esc	
Printer-friendly Version	
Interactive Discussion	



References

- Arakawa, A., Jung, J.-H., and Wu, C.-M.: Toward unification of the multiscale modeling of the atmosphere, *Atmos. Chem. Phys.*, 11, 3731–3742, doi:10.5194/acp-11-3731-2011, 2011. 7259
- 5 Banta, R. M., Pichugina, Y. L., and Brewer, W. A.: Turbulent velocity-variance profiles in the stable boundary layer generated by a nocturnal low-level jet, *J. Atmos. Sci.*, 63, 2700–2719, doi:10.1175/JAS3776.1, 2006. 7252
- Bretherton, C. S. and Park, S.: A new moist turbulence parameterization in the community atmosphere model, *J. Climate*, 22, 3422–3448, doi:10.1175/2008JCLI2556.1, 2009. 7255
- 10 Cakmur, R. V., Miller, R. L., and Torres, O.: Incorporating the effect of small-scale circulations upon dust emission in an atmospheric general circulation model, *J. Geophys. Res.-Atmos.*, 109, 7201, doi:10.1029/2003JD004067, 2004. 7253, 7259, 7267, 7276
- Capps, S. B. and Zender, C. S.: Observed and CAM3 GCM sea surface wind speed distributions: characterization, comparison, and bias reduction, *J. Climate*, 21, 6569, doi:10.1175/2008JCLI2374.1, 2008. 7265, 7271
- 15 Carta, J. A., Ramirez, P., and Velazquez, S.: A review of wind speed probability distributions used in wind energy analysis: case studies in the Canary Islands, *Renew. Sust. Energ. Rev.*, 13, 933–955, doi:10.1016/j.rser.2008.05.005, 2009. 7253
- Deardorff, J. W.: Preliminary results from numerical integrations of the unstable planetary boundary layer, *J. Atmos. Sci.*, 27, 1209–1210, doi:10.1175/1520-0469(1970)027<1209:PRFNIO>2.0.CO;2, 1970. 7252
- Dipankar, A., Stevens, B., Heinze, R., Moseley, C., Zängl, G., Giorgetta, M., and Brdar, S.: Large eddy simulation using the general circulation model ICON, *J. Adv. Model. Earth Syst.*, 07, doi:10.1002/2015MS000431 (online version), 2015. 7266
- 25 Durran, D. R.: Mountain waves and downslope winds, in: Atmospheric Processes Over Complex Terrain, edited by: Blumen, W., vol. 23 of Meteorological Monographs, American Meteorological Society, Boston, Massachusetts, 59–83, 1990. 7252
- ECMWF: European Centre for Medium-Range Weather Forecasts (ECMWF): IFS Documentation – Cy28r1, IV. Physical Processes, Tech. Report, European Centre for Medium-Range Weather Forecasts, ECMWF Research Department, Technical Memorandum Cy28r1, European Centre for Medium-Range Weather Forecast, Reading, UK, available at: <http://old.ecmwf.int/research/ifsdocs/CY28r1/index.html> (last access: 24 August 2015), 2004. 7267

Sub-grid wind-driven aerosol emissions in CAM5

K. Zhang et al.

[Title Page](#)

[Abstract](#)

[Introduction](#)

[Conclusions](#)

[References](#)

[Tables](#)

[Figures](#)



[Back](#)

[Close](#)

[Full Screen / Esc](#)

[Printer-friendly Version](#)

[Interactive Discussion](#)



Feng, Z., Hagos, S., Rowe, A. K., Burleyson, C. D., Martini, M. N., and de Szoeke, S. P.: Mechanisms of convective cloud organization by cold pools over tropical warm ocean during the AMIE/DYNAMO field campaign, *J. Adv. Model. Earth Syst.*, 7, 357–381, doi:10.1002/2014MS000384, 2015. 7252

- 5 Gettelman, A., Morrison, H., and Ghan, S. J.: A new two-moment bulk stratiform cloud microphysics scheme in the community atmosphere model, version 3 (CAM3). Part II: Single-column and global results, *J. Climate*, 21, 3660–3679, doi:10.1175/2008JCLI2116.1, 2008. 7254

10 Ghan, S. J. and Easter, R. C.: Comments on “A limited-area-model case study of the effects of sub-grid scale variations in relative humidity and cloud upon the direct radiative forcing of sulfate aerosol”, *Geophys. Res. Lett.*, 25, 1039–1040, doi:10.1029/98GL50357, 1998. 7251

Gläser, G., Kerkweg, A., and Wernli, H.: The Mineral Dust Cycle in EMAC 2.40: sensitivity to the spectral resolution and the dust emission scheme, *Atmos. Chem. Phys.*, 12, 1611–1627, doi:10.5194/acp-12-1611-2012, 2012. 7280

15 Godfrey, J. S. and Beljaars, A. C. M.: On the turbulent fluxes of buoyancy, heat and moisture at the air-sea interface at low wind speeds, *J. Geophys. Res.*, 96, 22043–22048, doi:10.1029/91JC02015, 1991. 7252, 7257

20 Grini, A. and Zender, C. S.: Roles of saltation, sandblasting, and wind speed variability on mineral dust aerosol size distribution during the Puerto Rican Dust Experiment (PRIDE), *J. Geophys. Res.*, 109, 7202, doi:10.1029/2003JD004233, 2004. 7259, 7265, 7271

Gustafson, W. I., Qian, Y., and Fast, J. D.: Downscaling aerosols and the impact of neglected subgrid processes on direct aerosol radiative forcing for a representative global climate model grid spacing, *J. Geophys. Res.-Atmos.*, 116, D13303, doi:10.1029/2010JD015480, 2011. 7251

25 Haywood, J. M., Ramaswamy, V., and Donner, L. J.: A limited-area-model case study of the effects of sub-grid scale variations in relative humidity and cloud upon the direct radiative forcing of sulfate aerosol, *Geophys. Res. Lett.*, 24, 143–146, doi:10.1029/96GL03812, 1997. 7251

30 Hourdin, F., Gueye, M., Diallo, B., Dufresne, J.-L., Escribano, J., Menut, L., Marticoréna, B., Siour, G., and Guichard, F.: Parameterization of convective transport in the boundary layer and its impact on the representation of the diurnal cycle of wind and dust emissions, *Atmos. Chem. Phys.*, 15, 6775–6788, doi:10.5194/acp-15-6775-2015, 2015. 7252

Sub-grid wind-driven aerosol emissions in CAM5

K. Zhang et al.

[Title Page](#)

[Abstract](#)

[Introduction](#)

[Conclusions](#)

[References](#)

[Tables](#)

[Figures](#)



[Back](#)

[Close](#)

[Full Screen / Esc](#)

[Printer-friendly Version](#)

[Interactive Discussion](#)



Sub-grid wind-driven aerosol emissions in CAM5

K. Zhang et al.

[Title Page](#)

[Abstract](#)

[Introduction](#)

[Conclusions](#)

[References](#)

[Tables](#)

[Figures](#)

◀

▶

◀

▶

[Back](#)

[Close](#)

[Full Screen / Esc](#)

[Printer-friendly Version](#)

[Interactive Discussion](#)



Huneeus, N., Schulz, M., Balkanski, Y., Griesfeller, J., Prospero, J., Kinne, S., Bauer, S., Boucher, O., Chin, M., Dentener, F., Diehl, T., Easter, R., Fillmore, D., Ghan, S., Ginoux, P., Grini, A., Horowitz, L., Koch, D., Krol, M. C., Landing, W., Liu, X., Mahowald, N., Miller, R., Morcrette, J.-J., Myhre, G., Penner, J., Perlitz, J., Stier, P., Takemura, T., and Zender, C. S.: Global dust model intercomparison in AeroCom phase I, *Atmos. Chem. Phys.*, 11, 7781–7816, doi:10.5194/acp-11-7781-2011, 2011. 7251

Iacono, M. J., Delamere, J. S., Mlawer, E. J., Shephard, M. W., Clough, S. A., and Collins, W. D.: Radiative forcing by long-lived greenhouse gases: calculations with the AER radiative transfer models, *J. Geophys. Res.*, 113, D13103, doi:10.1029/2008JD009944, 2008. 7255

Jabouille, P., Redelsperger, J. L., and Lafore, J. P.: Modification of surface fluxes by atmospheric convection in the TOGA COARE region, *Mon. Weather Rev.*, 124, 816–837, doi:10.1175/1520-0493(1996)124<0816:MOSFBA>2.0.CO;2, 1996. 7252

Jeuken, A., Siegmund, P., Heijboer, L., Feichter, J., and Bengtsson, L.: On the potential of assimilating meteorological analyses in a global climate model for the purposes of model validation, *J. Geophys. Res.*, 101, 16939–16950, doi:10.1029/96JD01218, 1996. 7273

Justus, C. G., Hargraves, W. R., Mikhail, A., and Graber, D.: Methods for estimating wind speed frequency distributions, *J. Appl. Meteorol.*, 17, 350–353, doi:10.1175/1520-0450(1978)017<0350:MFEWSF>2.0.CO;2, 1978. 7262, 7265, 7271

Justus, C. G., Mani, K., and Mikhail, A. S.: Interannual and month-to-month variations of wind speed, *J. Appl. Meteorol.*, 18, 913–920, doi:10.1175/1520-0450(1979)018<0913:IAMTMV>2.0.CO;2, 1979. 7253

Kooperman, G. J., Pritchard, M. S., Ghan, S. J., Wang, M., Somerville, R. C. J., and Russell, L. M.: Constraining the influence of natural variability to improve estimates of global aerosol indirect effects in a nudged version of the Community Atmosphere Model 5, *J. Geophys. Res.*, 117, D23204, doi:10.1029/2012JD018588, 2012. 7274

Lawrence, D. M., Oleson, K. W., Flanner, M. G., Thornton, P. E., Swenson, S. C., Lawrence, P. J., Zeng, X., Yang, Z.-L., Levis, S., Sakaguchi, K., Bonan, G. B., and Slater, A. G.: Parameterization improvements and functional and structural advances in Version 4 of the Community Land Model, *J. Adv. Model. Earth Syst.*, 3, M03001, doi:10.1029/2011MS000045, 2011. 7255

Lin, S.-J.: A “Vertically Lagrangian” finite-volume dynamical core for global models, *Mon. Weather Rev.*, 132, 2293–2307, doi:10.1175/1520-0493(2004)132<2293:AVLFDC>2.0.CO;2, 2004. 7254

Sub-grid wind-driven aerosol emissions in CAM5

K. Zhang et al.

- Liu, X., Easter, R. C., Ghan, S. J., Zaveri, R., Rasch, P., Shi, X., Lamarque, J.-F., Gettelman, A., Morrison, H., Vitt, F., Conley, A., Park, S., Neale, R., Hannay, C., Ekman, A. M. L., Hess, P., Mahowald, N., Collins, W., Iacono, M. J., Bretherton, C. S., Flanner, M. G., and Mitchell, D.: Toward a minimal representation of aerosols in climate models: description and evaluation in the Community Atmosphere Model CAM5, *Geosci. Model Dev.*, 5, 709–739, doi:10.5194/gmd-5-709-2012, 2012a. 7254, 7256
- Liu, X., Shi, X., Zhang, K., Jensen, E. J., Gettelman, A., Barahona, D., Nenes, A., and Lawson, P.: Sensitivity studies of dust ice nuclei effect on cirrus clouds with the Community Atmosphere Model CAM5, *Atmos. Chem. Phys.*, 12, 12061–12079, doi:10.5194/acp-12-12061-2012, 2012b. 7278
- Lumley, J. L. and Panofsky, H. A.: The Structure of Atmospheric Turbulence, Interscience Monographs and Texts in Physics and Astronomy, Interscience Publishers, New York, p. 239, 1964. 7252
- Lunt, D. J. and Valdes, P. J.: The modern dust cycle: comparison of model results with observations and study of sensitivities, *J. Geophys. Res.*, 107, 4669, doi:10.1029/2002JD002316, 2002. 7252, 7257, 7267
- Ma, P.-L., Rasch, P. J., Fast, J. D., Easter, R. C., Gustafson Jr., W. I., Liu, X., Ghan, S. J., and Singh, B.: Assessing the CAM5 physics suite in the WRF-Chem model: implementation, resolution sensitivity, and a first evaluation for a regional case study, *Geosci. Model Dev.*, 7, 755–778, doi:10.5194/gmd-7-755-2014, 2014. 7260
- Mahoney, W. P.: Gust front characteristics and the kinematics associated with interacting thunderstorm outflows, *Mon. Weather Rev.*, 116, 1474–1492, doi:10.1175/1520-0493(1988)116<1474:GFCATK>2.0.CO;2, 1988. 7252
- Marcella, M. P. and Eltahir, E. A. B.: Effects of mineral aerosols on the summertime climate of southwest Asia: incorporating subgrid variability in a dust emission scheme, *J. Geophys. Res.-Atmos.*, 115, 18203, doi:10.1029/2010JD014036, 2010. 7253
- Mårtensson, E. M., Nilsson, E. D., de Leeuw, G., Cohen, L. H., and Hansson, H.-C.: Laboratory simulations and parameterization of the primary marine aerosol production, *J. Geophys. Res.-Atmos.*, 108, 4297, doi:10.1029/2002JD002263, 2003. 7255
- Menut, L.: Sensitivity of hourly Saharan dust emissions to NCEP and ECMWF modeled wind speed, *J. Geophys. Res.-Atmos.*, 113, D16201, doi:10.1029/2007JD009522, 2008. 7265

[Title Page](#)

[Abstract](#)

[Introduction](#)

[Conclusions](#)

[References](#)

[Tables](#)

[Figures](#)

◀

▶

◀

▶

[Back](#)

[Close](#)

[Full Screen / Esc](#)

[Printer-friendly Version](#)

[Interactive Discussion](#)



Mlawer, E. J., Taubman, S. J., Brown, P. D., Iacono, M. J., and Clough, S. A.: Radiative transfer for inhomogeneous atmospheres: RRTM, a validated correlated-k model for the longwave, *J. Geophys. Res.*, 102, 16663–16682, doi:10.1029/97JD00237, 1997. 7255

Monahan, A. H.: The probability distribution of sea surface wind speeds. Part II: Dataset intercomparison and seasonal variability, *J. Climate*, 19, 521, doi:10.1175/JCLI3641.1, 2006. 5 7253

Morrison, H. and Gettelman, A.: A new two-moment bulk stratiform cloud microphysics scheme in the NCAR Community Atmosphere Model (CAM3), Part I: description and numerical tests, *J. Climate*, 21, 3642–3659, doi:10.1175/2008JCLI2105.1, 2008. 7254

10 Neale, R. B., Chen, C. C., Gettelman, A., Lauritzen, P. H., Park, S., Williamson, D. L., Conley, A. J., Garcia, R., Kinnison, D., Lamarque, J. F., Marsh, D., Mills, M., Smith, A. K., Tilmes, S., Vitt, F., Morrison, H., Cameron-Smith, P., Collins, W. D., Iacono, M. J., Easter, R. C., Ghan, S. J., Liu, X. H., Rasch, P. J., and Taylor, M. A.: Description of the NCAR Community Atmosphere Model (CAM5.0), Tech. Rep. NCAR/TN-486-STR, National Center for Atmospheric Research, Boulder, CO, USA, available at: <http://www.cesm.ucar.edu/models/cesm1.0/cam/> (last access: 24 August 2015), 2010. 7255

15 Oleson, K., Lawrence, D., Bonan, G., Flanner, M., Kluzeck, E., Lawrence, P., Levis, S., Swenson, S., Thornton, P., Dai, A., Decker, M., Dickinson, R., Feddema, J., Heald, C., Hoffman, F., Lamarque, J.-F., Mahowald, N., Niu, G.-Y., Qian, T., Randerson, J., Running, S., Sakaguchi, K., Slater, A., Stockli, R., Wang, A., Yang, Z.-L., Zeng, X., and Zeng, X.: Technical Description of version 4.0 of the Community Land Model (CLM), Tech. Rep. NCAR/TN-478+STR, National Center for Atmospheric Research, Boulder, CO, USA, available at: <http://www.cesm.ucar.edu/models/cesm1.0/clm/> (last access: 24 August 2015), 2010. 7255, 7256

20 25 Panofsky, H., Tennekes, H., Lenschow, D., and Wyngaard, J.: The characteristics of turbulent velocity components in the surface layer under convective conditions, *Bound.-Lay. Meteorol.*, 11, 355–361, doi:10.1007/BF02186086, 1977. 7252

Park, S.: A unified convection scheme (UNICON). part I: formulation, *J. Atmos. Sci.*, 71, 3902–3930, doi:10.1175/JAS-D-13-0234.1, 2014. 7264

30 Park, S. and Bretherton, C. S.: The University of Washington shallow convection and moist turbulence schemes and their impact on climate simulations with the Community Atmosphere Model, *J. Climate*, 22, 3449–3469, doi:10.1175/2008JCLI2557.1, 2009. 7254

Sub-grid wind-driven aerosol emissions in CAM5

K. Zhang et al.

[Title Page](#)

[Abstract](#)

[Introduction](#)

[Conclusions](#)

[References](#)

[Tables](#)

[Figures](#)



[Back](#)

[Close](#)

[Full Screen / Esc](#)

[Printer-friendly Version](#)

[Interactive Discussion](#)



Pavia, E. G. and O'Brien, J. J.: Weibull statistics of wind speed over the ocean., *J. Appl. Meteorol.*, 25, 1324–1332, doi:10.1175/1520-0450(1986)025<1324:WSOWSO>2.0.CO;2, 1986. 7253

Prospero, J. M., Ginoux, P., Torres, O., Nicholson, S. E., and Gill, T. E.: Environmental characterization of global sources of atmospheric soil dust identified with the NIMBUS 7 Total Ozone Mapping Spectrometer (TOMS) absorbing aerosol product, *Rev. Geophys.*, 40, 1002, doi:10.1029/2000RG000095, 2002. 7310

Qian, Y., Gustafson Jr., W. I., and Fast, J. D.: An investigation of the sub-grid variability of trace gases and aerosols for global climate modeling, *Atmos. Chem. Phys.*, 10, 6917–6946, doi:10.5194/acp-10-6917-2010, 2010. 7251

Redelsperger, J.-L., Guichard, F., and Mondon, S.: A parameterization of mesoscale enhancement of surface fluxes for large-scale models, *J. Climate*, 13, 402–421, doi:10.1175/1520-0442(2000)013<0402:APOME>2.0.CO;2, 2000. 7252, 7267, 7268, 7269, 7275, 7276, 7303

Ridley, D. A., Heald, C. L., Pierce, J. R., and Evans, M. J.: Toward resolution-independent dust emissions in global models: impacts on the seasonal and spatial distribution of dust, *Geophys. Res. Lett.*, 40, 2873–2877, doi:10.1002/grl.50409, 2013. 7262

Schumann, U.: Minimum friction velocity and heat transfer in the rough surface layer of a convective boundary layer, *Bound.-Lay. Meteorol.*, 44, 311–326, doi:10.1007/BF00123019, 1988. 7252

Skamarock, W. and Klemp, J.: A time-split nonhydrostatic atmospheric model for weather research and forecasting applications, *J. Comput. Phys.*, 227, 3465–3485, doi:10.1016/j.jcp.2007.01.037, 2008. 7260

Stevens, R. G. and Pierce, J. R.: A parameterization of sub-grid particle formation in sulfur-rich plumes for global- and regional-scale models, *Atmos. Chem. Phys.*, 13, 12117–12133, doi:10.5194/acp-13-12117-2013, 2013. 7251

Stier, P., Seinfeld, J. H., Kinne, S., and Boucher, O.: Aerosol absorption and radiative forcing, *Atmos. Chem. Phys.*, 7, 5237–5261, doi:10.5194/acp-7-5237-2007, 2007. 7278

Textor, C., Schulz, M., Guibert, S., Kinne, S., Balkanski, Y., Bauer, S., Berntsen, T., Berglen, T., Boucher, O., Chin, M., Dentener, F., Diehl, T., Easter, R., Feichter, H., Fillmore, D., Ghan, S., Ginoux, P., Gong, S., Grini, A., Hendricks, J., Horowitz, L., Huang, P., Isaksen, I., Iversen, I., Kloster, S., Koch, D., Kirkevåg, A., Kristjansson, J. E., Krol, M., Lauer, A., Lamarque, J. F., Liu, X., Montanaro, V., Myhre, G., Penner, J., Pitari, G., Reddy, S., Seland, Ø., Stier, P., 30

Sub-grid wind-driven aerosol emissions in CAM5

K. Zhang et al.

[Title Page](#)

[Abstract](#)

[Introduction](#)

[Conclusions](#)

[References](#)

[Tables](#)

[Figures](#)



[Back](#)

[Close](#)

[Full Screen / Esc](#)

[Printer-friendly Version](#)

[Interactive Discussion](#)



Takemura, T., and Tie, X.: Analysis and quantification of the diversities of aerosol life cycles within AeroCom, *Atmos. Chem. Phys.*, 6, 1777–1813, doi:10.5194/acp-6-1777-2006, 2006. 7251

5 Torres, O., Bhartia, P. K., Herman, J. R., Sinyuk, A., Ginoux, P., and Holben, B.: A long-term record of aerosol optical depth from TOMS observations and comparison to AERONET measurements, *J. Atmos. Sci.*, 59, 398–413, doi:10.1175/1520-0469(2002)059<0398:ALTROA>2.0.CO;2, 2002. 7310

10 Westphal, D. L., Toon, O. B., and Carlson, T. N.: A case study of mobilization and transport of Saharan dust, *J. Atmos. Sci.*, 45, 2145–2175, doi:10.1175/1520-0469(1988)045<2145:ACSOMA>2.0.CO;2, 1988. 7251

White, B.: Soil transport by winds on Mars, *J. Geophys. Res.*, 84, 4643–4651, doi:10.1029/JB084iB09p04643, 1979. 7257

Zender, C. S. and Kwon, E. Y.: Regional contrasts in dust emission responses to climate, *J. Geophys. Res.-Atmos.*, 110, D13201, doi:10.1029/2004JD005501, 2005. 7277, 7310

15 Zender, C. S., Bian, H., and Newman, D.: The mineral Dust Entrainment And Deposition (DEAD) model: description and 1990s dust climatology, *J. Geophys. Res.*, 108, 4416, doi:10.1029/2002JD002775, 2003. 7256, 7305

20 Zeng, X., Zhang, Q., Johnson, D., and Tao, W.-K.: Parameterization of wind gustiness for the computation of ocean surface fluxes at different spatial scales, *Mon. Weather Rev.*, 130, 2125–2133, doi:10.1175/1520-0493(2002)130<2125:POWGFT>2.0.CO;2, 2002. 7252, 7267, 7272

Zhang, G. J. and McFarlane, N. A.: Sensitivity of climate simulations to the parameterization of cumulus convection in the Canadian Climate Centre general circulation model, *Atmos. Ocean*, 33, 407–446, doi:10.1080/07055900.1995.9649539, 1995. 7254

25 Zhang, K., O'Donnell, D., Kazil, J., Stier, P., Kinne, S., Lohmann, U., Ferrachat, S., Croft, B., Quaas, J., Wan, H., Rast, S., and Feichter, J.: The global aerosol-climate model ECHAM-HAM, version 2: sensitivity to improvements in process representations, *Atmos. Chem. Phys.*, 12, 8911–8949, doi:10.5194/acp-12-8911-2012, 2012. 7258

30 Zhang, K., Liu, X., Wang, M., Comstock, J. M., Mitchell, D. L., Mishra, S., and Mace, G. G.: Evaluating and constraining ice cloud parameterizations in CAM5 using aircraft measurements from the SPARTICUS campaign, *Atmos. Chem. Phys.*, 13, 4963–4982, doi:10.5194/acp-13-4963-2013, 2013. 7278

Sub-grid wind-driven
aerosol emissions in
CAM5

K. Zhang et al.

Title Page

Abstract

Introduction

Conclusions

References

Tables

Figures

◀

▶

◀

▶

Back

Close

Full Screen / Esc

Printer-friendly Version

Interactive Discussion



Sub-grid wind-driven
aerosol emissions in
CAM5

K. Zhang et al.

[Title Page](#)

[Abstract](#)

[Introduction](#)

[Conclusions](#)

[References](#)

[Tables](#)

[Figures](#)



[Back](#)

[Close](#)

[Full Screen / Esc](#)

[Printer-friendly Version](#)

[Interactive Discussion](#)



Sub-grid wind-driven aerosol emissions in CAM5

K. Zhang et al.

Table 1. List of CAM5 simulations discussed in Sect. 5. DU and SS refer to dust and sea salt emissions, respectively. “With PDF” means the Weibull distribution of wind speed is used in the emission calculations (cf. Sect. 2.5). “Without PDF” means the enhancement of grid-box mean wind speed is taken into account, but the emission calculations use only the (enhanced) mean wind speed, not the Weibull PDF.

Simulation	Source of sub-grid wind variability				Dust emission factor
	Turbulence (Eq. 20)	Dry convective eddy (Eq. 21)	Moist convective eddy (ocean, Eqs. 23 and 24)	Meso-scale flows over topography (land, Eqs. 26 and 27)	
NOSG	–	–	–	–	0.35^{-1}
CTRL	–	DU; Without PDF	–	–	0.35^{-1}
EXP1	–	DU + SS; With PDF	–	–	0.35^{-1}
EXP2	DU + SS; With PDF	DU + SS; With PDF	–	–	0.35^{-1}
EXP3	DU + SS; With PDF	DU + SS; With PDF	DU + SS; With PDF	DU + SS; With PDF	0.35^{-1}
EXP4	DU + SS; With PDF	DU + SS; With PDF	DU + SS; With PDF	DU + SS; With PDF	0.57^{-1}

- [Title Page](#)
- [Abstract](#) | [Introduction](#)
- [Conclusions](#) | [References](#)
- [Tables](#) | [Figures](#)
- [◀](#) | [▶](#)
- [◀](#) | [▶](#)
- [Back](#) | [Close](#)
- [Full Screen / Esc](#)
- [Printer-friendly Version](#)
- [Interactive Discussion](#)



Sub-grid wind-driven aerosol emissions in CAM5

K. Zhang et al.

Table 2. Simulated annual mean global and regional sea salt emissions (Tg yr^{-1}) for the year 2006. Numbers in parenthesis are the relative differences with respect to the default model (CTRL). Meanings of the simulation short names are explained in Table 1. NOSG and EXP4 are not included here because both are identical to CTRL in terms of the sea salt emission parameterization.

Simulation	Global	Northern Hemisphere (30–60° N)	Southern Hemisphere (30–60° S)	Tropics (20° S–20° N)
CTRL	5011.3	854.8	2504.8	925.8
EXP1	5024.8 (+0.27 %)	856.8 (+0.24 %)	2514.2 (+0.38 %)	926.4 (+0.07 %)
EXP2	5185.6 (+3.48 %)	886.7 (+3.74 %)	2580.1 (+3.00 %)	964.6 (+4.19 %)
EXP3	5372.3 (+7.20 %)	925.4 (+8.26 %)	2666.2 (+6.44 %)	1002.5 (+8.29 %)

[Title Page](#)[Abstract](#)[Introduction](#)[Conclusions](#)[References](#)[Tables](#)[Figures](#)[Back](#)[Close](#)[Full Screen / Esc](#)[Printer-friendly Version](#)[Interactive Discussion](#)

Sub-grid wind-driven aerosol emissions in CAM5

K. Zhang et al.

Table 3. Simulated annual mean global and regional dust emission (Tg yr^{-1}) for the year 2006. Numbers in parenthesis are the relative differences with respect to the default model (CTRL). The experiment configurations are explained in Table 1.

Simulation	Global	North Africa (10–30° N, 20° W–40° E)	East Asia (30–50° N, 80–120° E)	West Asia (15–50° N, 40–70° E)	Australia (10–40° S, 110–140° E)	North America (10–60° N, 30–140° W)	South America (0–60° S, 40–80° W)
NOSG	3365.0 (−14.3 %)	1588.4 (−15.6 %)	551.8 (−13.7 %)	522.4 (−15.6 %)	137.5 (−11.8 %)	1.74 (−24.0 %)	7.57 (−39.4 %)
CTRL	3927.9	1880.7	639.3	619.3	155.9	2.29	12.5
EXP1	5000.6 (+27.3 %)	2441.2 (+29.8 %)	864.0 (+35.2 %)	828.4 (+33.8 %)	150.5 (−3.5 %)	3.79 (+65.4 %)	29.0 (+132.2 %)
EXP2	5120.9 (+30.4 %)	2492.2 (+32.5 %)	877.5 (+37.3 %)	848.8 (+37.1 %)	161.6 (3.6 %)	3.89 (+70.1 %)	29.5 (+135.5 %)
EXP3	6023.7 (+53.4 %)	2737.9 (+45.6 %)	1127.4 (+76.4 %)	1048.1 (+69.2 %)	177.7 (+13.9 %)	5.10 (+122.9 %)	45.2 (+261.7 %)
EXP4	4023.5 (+2.43 %)	1826.8 (−2.87 %)	802.1 (+25.5 %)	687.0 (+10.9 %)	109.8 (−29.6 %)	3.16 (+38.0 %)	28.0 (+123.9 %)

- [Title Page](#)
- [Abstract](#) | [Introduction](#)
- [Conclusions](#) | [References](#)
- [Tables](#) | [Figures](#)
- [◀](#) | [▶](#)
- [◀](#) | [▶](#)
- [Back](#) | [Close](#)
- [Full Screen / Esc](#)
- [Printer-friendly Version](#)
- [Interactive Discussion](#)



Sub-grid wind-driven aerosol emissions in CAM5

K. Zhang et al.

Table 4. Definition of the 14 major dust source regions in which the simulated and MISR retrieved AOD are compared in Fig. 15. The relative differences between the simulated and MISR retrieved AOD are also shown.

Number	Region	MISR	CTRL vs. MISR	EXP3 vs. MISR	EXP4 vs. MISR
1	Eastern Sahel (10–15° N, 10° W–20° E)	0.243	−11.1 %	+6.17 %	−9.47 %
2	Bodele Depression (15–20° N, 10–20° E)	0.526	−7.03 %	+33.1 %	−6.46 %
3	Western US and Mexico (25–35° N, 110–100° W)	0.147	−57.8 %	−56.5 %	−57.1 %
4	Lake Eyre Basin (30–25° S, 136–145° E)	0.130	+16.2 %	+32.3 %	−0.77 %
5	Botswana (25–20° S, 20–30° E)	0.157	−40.8 %	−38.9 %	−43.3 %
6	Gobi Desert (42.5–45° N, 105–110° E)	0.219	−5.48 %	+63.5 %	+16.4 %
7	Chinese Loess Plateau (32.5–37.5° N, 105–110° E)	0.385	−22.9 %	+9.87 %	−14.8 %
8	Great Salt Lake (40–42.5° N, 115–112.5° W)	0.156	−76.9 %	−75.6 %	−76.3 %
9	Zone of Chotts (32.5–35° N, 5–10° E)	0.312	+56.1 %	+167.0 %	+85.6 %
10	Tigris Euphrates (27.5–32.5° N, 45–57.5° E)	0.320	+1.56 %	+58.4 %	+11.3 %
11	Saudi Arabia (20–25° N, 47.5–52.5° E)	0.501	−12.6 %	+29.7 %	−7.58 %
12	Oman (17.5–20° N, 52.5–57.5° E)	0.388	+1.80 %	+47.9 %	+6.19 %
13	Tarim Basin (35–40° N, 75–90° E)	0.347	−30.8 %	+27.4 %	−4.32 %
14	Thar Desert (25–30° N, 70–75° E)	0.421	−24.0 %	+11.6 %	−15.9 %



Sub-grid wind-driven aerosol emissions in CAM5

K. Zhang et al.

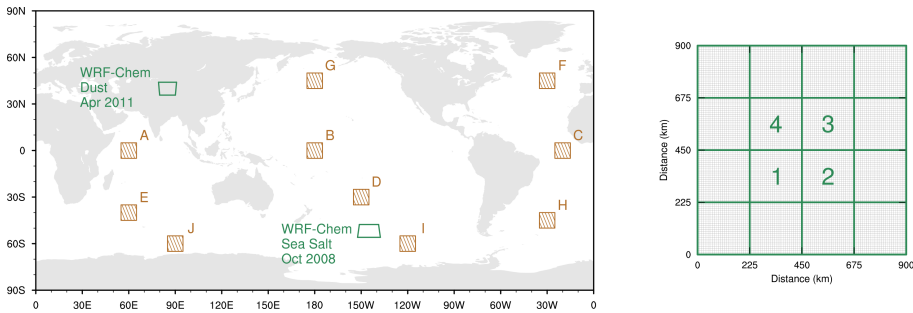


Figure 1. Left panel indicates the two $900\text{ km} \times 900\text{ km}$ WRF domains (green), and the ten $10^\circ\text{ lat} \times 10^\circ\text{ lon}$ regions (brown) in which the estimated sub-grid wind variabilities are evaluated in Fig. 8. Right panel shows the four imagined 225 km grid boxes (label as 1–4) in each of the WRF domains shown in the left panel. The 225 km grid boxes are used for the offline estimates in Figs. 4 and 6, as well as the evaluations in Figs. 9 and 11.

Sub-grid wind-driven aerosol emissions in CAM5

K. Zhang et al.

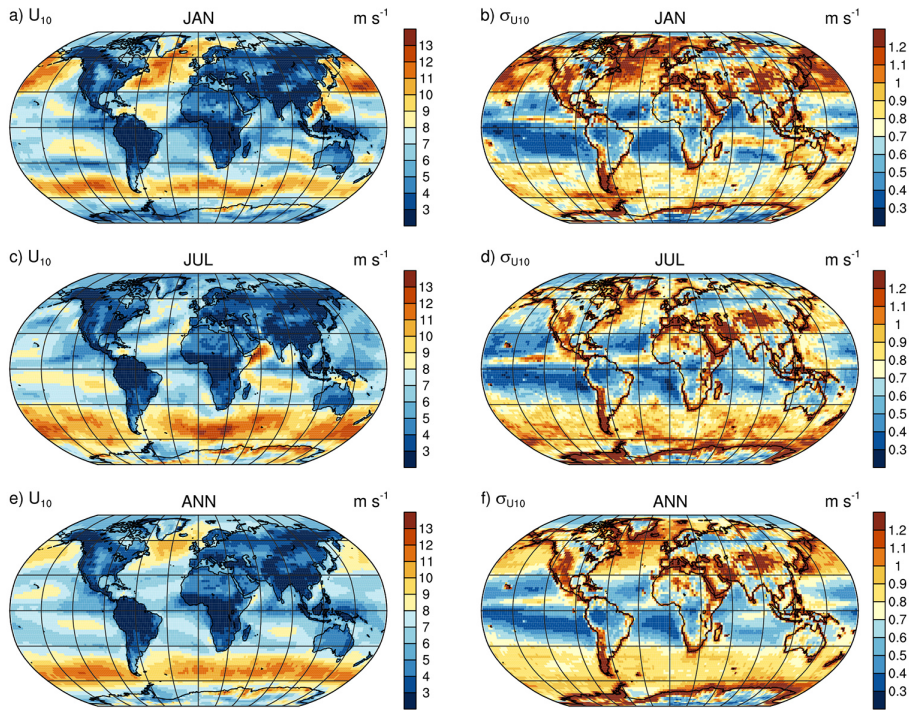


Figure 2. Grid-box average (left column) and sub-grid standard deviation (right column) of the 10 m wind speed, diagnosed on an imagined $2^\circ \times 2^\circ$ horizontal grid from the ECMWF 15 km global analysis. From top to bottom: January average, July average, and annual mean. See Sect. 3 for further details.

Title Page

Abstract

Introduction

Conclusions

References

Tables

Figures



Back

Close

Full Screen / Esc

[Printer-friendly Version](#)

Interactive Discussion



Sub-grid wind-driven aerosol emissions in CAM5

K. Zhang et al.

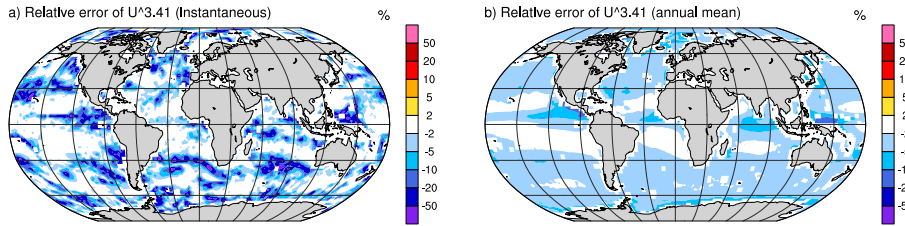


Figure 3. Relative error of $U_{10}^{3.41}$ over the ocean, caused by ignoring sub-grid wind variability. The quantity shown is the relative error of Eq. (10) with respect to Eq. (11), calculated on an imagined $2^\circ \times 2^\circ$ horizontal grid using the ECMWF 15 km global analysis. Left panel shows the instantaneous results at an arbitrarily chosen time (00:00 GMT on 1 January 2011). Right panel shows the relative error of the year 2011 annual mean.

[Title Page](#)[Abstract](#)[Introduction](#)[Conclusions](#)[References](#)[Tables](#)[Figures](#)[Back](#)[Close](#)[Full Screen / Esc](#)[Printer-friendly Version](#)[Interactive Discussion](#)

Sub-grid wind-driven aerosol emissions in CAM5

K. Zhang et al.

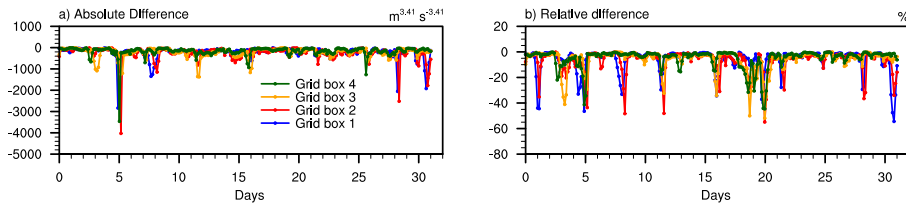


Figure 4. Time series of the error of $U_{10}^{3.41}$ in the four $225\text{ km} \times 225\text{ km}$ grid boxes in the WRF domain over the Southern Ocean (cf. Fig. 1 and Sect. 3). The absolute (left) and relative (right) errors are calculated for Eq. (10) assuming Eq. (11) is the “truth”.

- [Title Page](#)
- [Abstract](#) [Introduction](#)
- [Conclusions](#) [References](#)
- [Tables](#) [Figures](#)
- [◀](#) [▶](#)
- [◀](#) [▶](#)
- [Back](#) [Close](#)
- [Full Screen / Esc](#)
- [Printer-friendly Version](#)
- [Interactive Discussion](#)

Sub-grid wind-driven aerosol emissions in **CAM5**

K. Zhang et al.

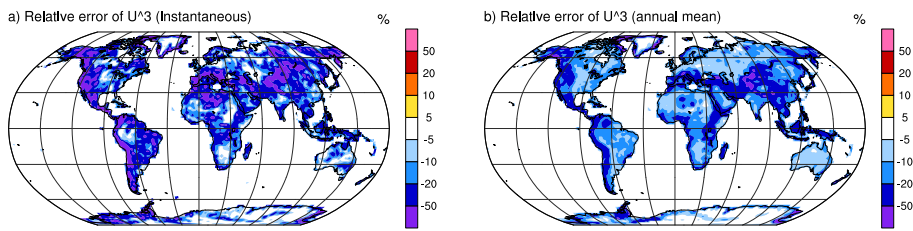


Figure 5. As in Fig. 3 but for the relative errors of U_{10}^3 over land. The errors are calculated for Eq. (12) assuming Eq. (13) is the “truth”.

Title Page

Abstract

Introduction

Conclusions

References

Tables

Figures



Back

Close

Full Screen / Esc

[Printer-friendly Version](#)

Interactive Discussion



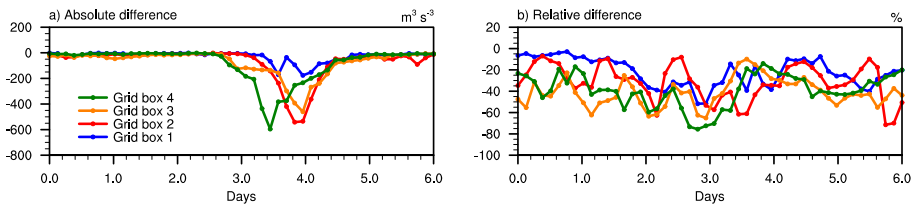


Figure 6. As in Fig. 4 but for the WRF simulation over Western China, and for the error of U_{10}^3 . The errors are calculated for Eq. (12) assuming Eq. (13) is the “truth”.

Title Page

Abstract

Introduction

Conclusions

References

Tables

Figures



Back

Close

Full Screen / Esc

[Printer-friendly Version](#)

Interactive Discussion



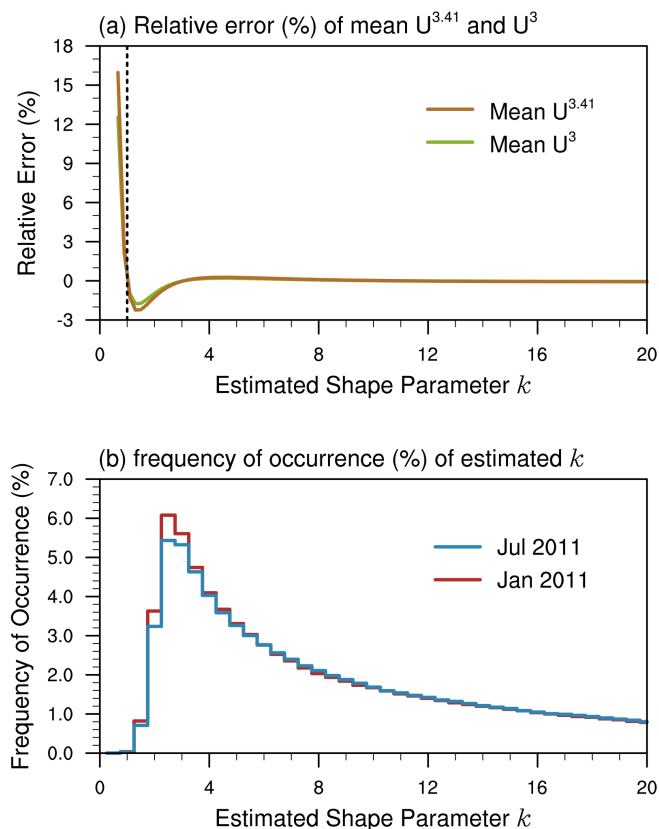


Figure 7. (a) Relative error in $\overline{U_{10}^{3.41}}$ and $\overline{U_{10}^3}$ as a result of estimating the shape and scale parameters of a Weibull distribution using Eqs. (15) and (16). **(b)** Histograms of the Weibull shape parameter k estimated with Eq. (15) using 6 hourly ECMWF analysis of January and July 2011 for imagined 2° grid boxes. Further details can be found in Sect. 4.1.

Sub-grid wind-driven aerosol emissions in CAM5

K. Zhang et al.

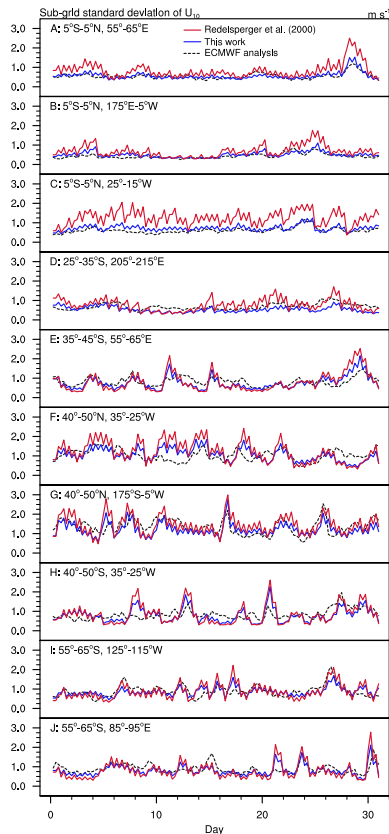


Figure 8. Time series of the sub-grid standard deviation of U_{10} (ms^{-1}) in January 2012 averaged over the $10^\circ \times 10^\circ$ hatched boxes in Fig. 1. Dashed black curves are directly diagnosed from the ECMWF surface wind data. Solid blue and red curves are the $\sigma_{U,m}$ calculated using the ECMWF precipitation rates and the empirical formulas of this study (Eq. 23) and Redelsperger et al. (2000) (Eq. 22), respectively.

Printer-friendly Version

Interactive Discussion

Title Page

Abstract

Introduction

Conclusions

References

Tables

Figures



Back

Close

Full Screen / Esc

Sub-grid wind-driven aerosol emissions in CAM5

K. Zhang et al.

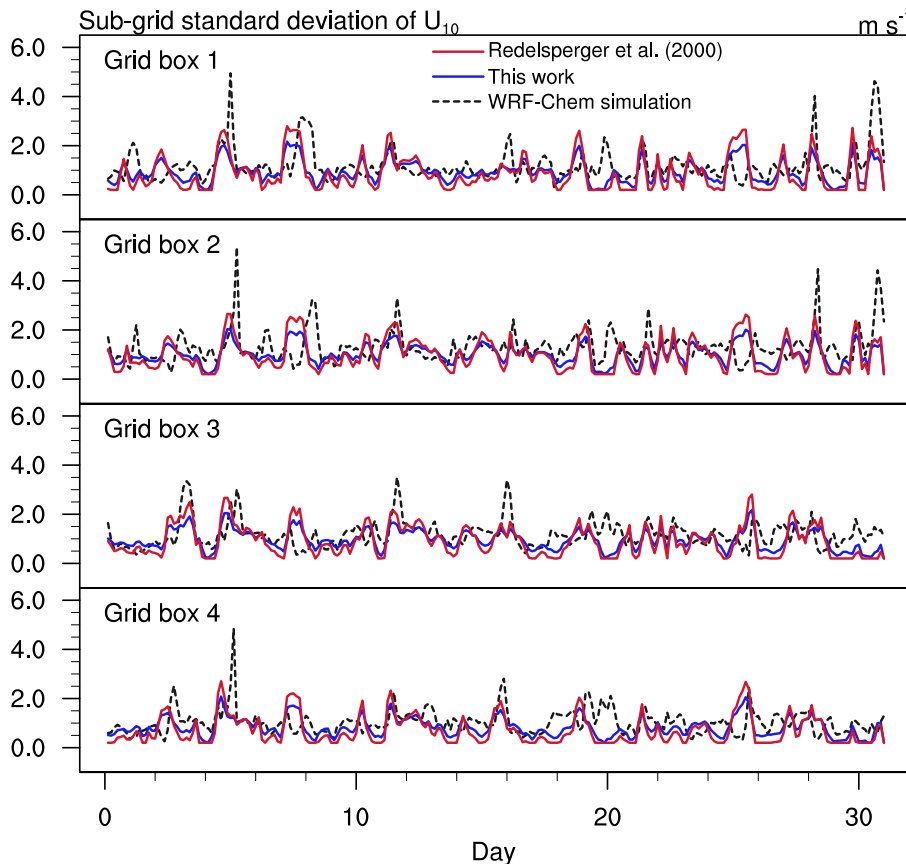
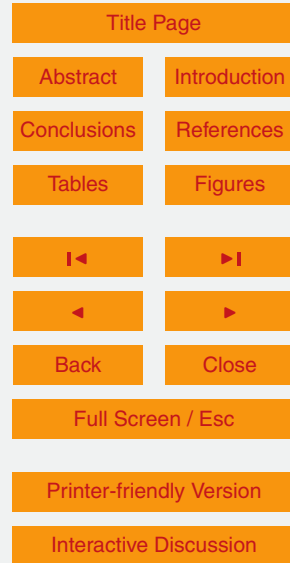


Figure 9. As in Fig. 8 but evaluating Eqs. (23) and (22) using the WRF simulation over the Southern Ocean. The domain of the WRF simulation and the location of the four imagined 225 km × 225 km grid cells are illustrated in Fig. 1.

Sub-grid wind-driven aerosol emissions in CAM5

K. Zhang et al.

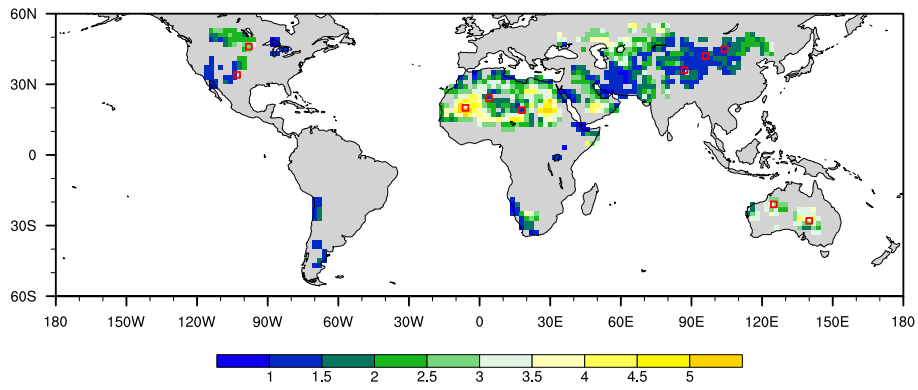


Figure 10. Geographical distribution of the coefficient C (unitless) derived for a 2° lat \times 2° lon GCM grid using the ECMWF 15 km analysis of the year 2011 and Eq. (26). The locations with no results are either covered by land ice or lake, or associated with leaf area indices (LAI) larger than 0.3 throughout the year, thus cannot have dust emission according to the parameterization of Zender et al. (2003) and the land surface characteristics data used in the CAM5 simulations in this paper. The red boxes correspond to the panels in Fig. 11 in which the time series of sub-grid wind variability are analyzed.

[Title Page](#)[Abstract](#)[Introduction](#)[Conclusions](#)[References](#)[Tables](#)[Figures](#)[◀](#)[▶](#)[◀](#)[▶](#)[Back](#)[Close](#)[Full Screen / Esc](#)[Printer-friendly Version](#)[Interactive Discussion](#)

Sub-grid wind-driven aerosol emissions in CAM5

K. Zhang et al.

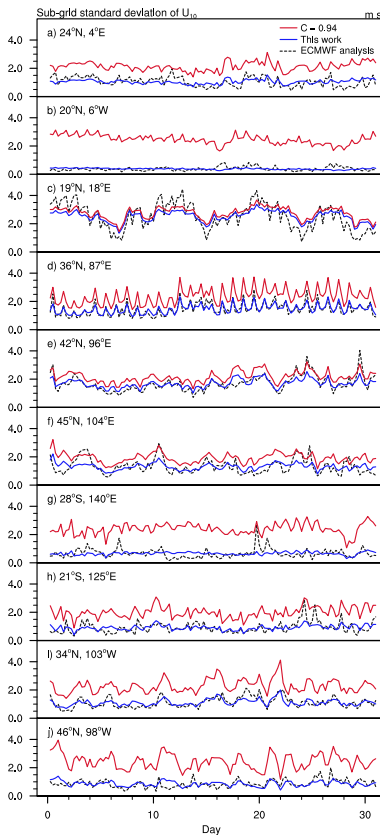


Figure 11. Time series of the sub-grid standard deviation of U_{10} (ms^{-1}) in January 2012 in the $2^\circ \text{lat} \times 2^\circ \text{lon}$ grid cells indicated by red boxes in Fig. 10. Dashed black curves are results derived from the ECMWF 15 km analysis. Red curves are results estimated using Eq. (27) with $C = 0.94$. Blue curves are also estimates using Eq. (27), but with location dependent C calculated from Eq. (26).

Sub-grid wind-driven aerosol emissions in CAM5

K. Zhang et al.

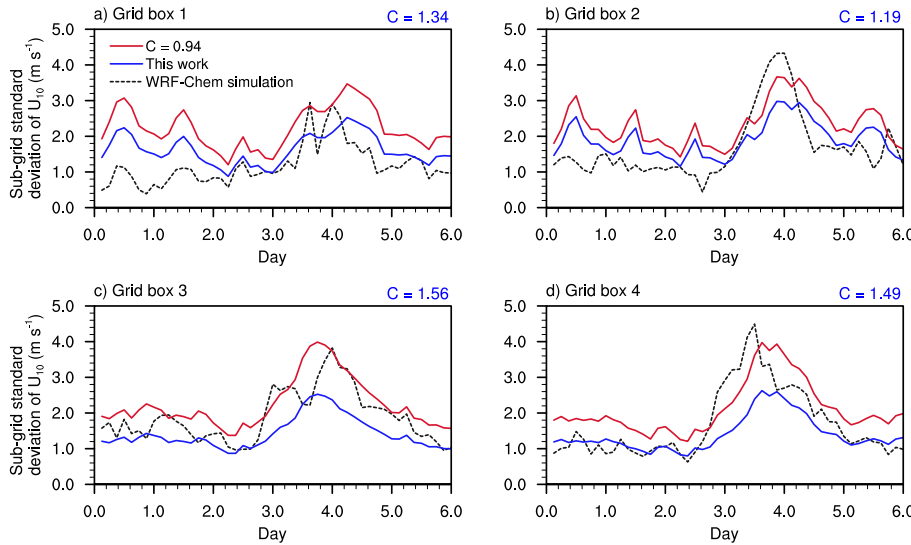


Figure 12. As in Fig. 11, but for the four 225 km boxes at the center of the WRF domain near the Taklamakan Desert. The C values used for the blue curves are derived from the ECMWF analysis of year 2011 for $2^\circ \text{ lat} \times 2^\circ \text{ lon}$ grid cells that are closest to the 225 km boxes.

[Title Page](#)

[Abstract](#)

[Introduction](#)

[Conclusions](#)

[References](#)

[Tables](#)

[Figures](#)

◀

▶

◀

▶

[Back](#)

[Close](#)

[Full Screen / Esc](#)

[Printer-friendly Version](#)

[Interactive Discussion](#)

Sub-grid wind-driven aerosol emissions in CAM5

K. Zhang et al.

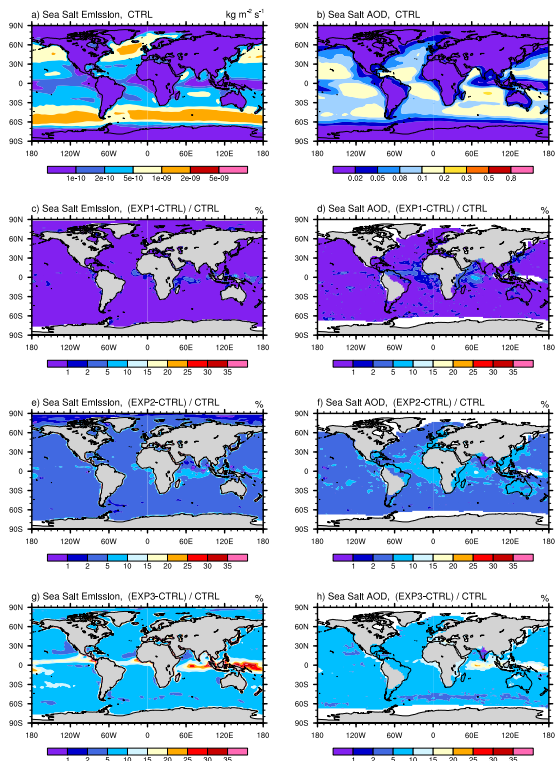


Figure 13. Top row: year 2006 mean sea salt emission flux ($\text{kg m}^{-2} \text{s}^{-1}$) and AOD (unitless, sea salt only) in the nudged CAM5 simulation (CTRL); lower rows: relative differences of sea salt emission and AOD between the sensitivity experiments and the CTRL simulation. In the lower three panels of the left column, locations that are masked out (white or gray) have emission fluxes less than $1 \times 10^{-12} \text{ kg m}^{-2} \text{s}^{-1}$ in the default model. In the lower panels of the right column, the masked out locations have sea salt AOD < 0.01 in CTRL.



Sub-grid wind-driven aerosol emissions in CAM5

K. Zhang et al.

[Title Page](#)

[Abstract](#)

[Introduction](#)

[Conclusions](#)

[References](#)

[Tables](#)

[Figures](#)



[Back](#)

[Close](#)

[Full Screen / Esc](#)

[Printer-friendly Version](#)

[Interactive Discussion](#)

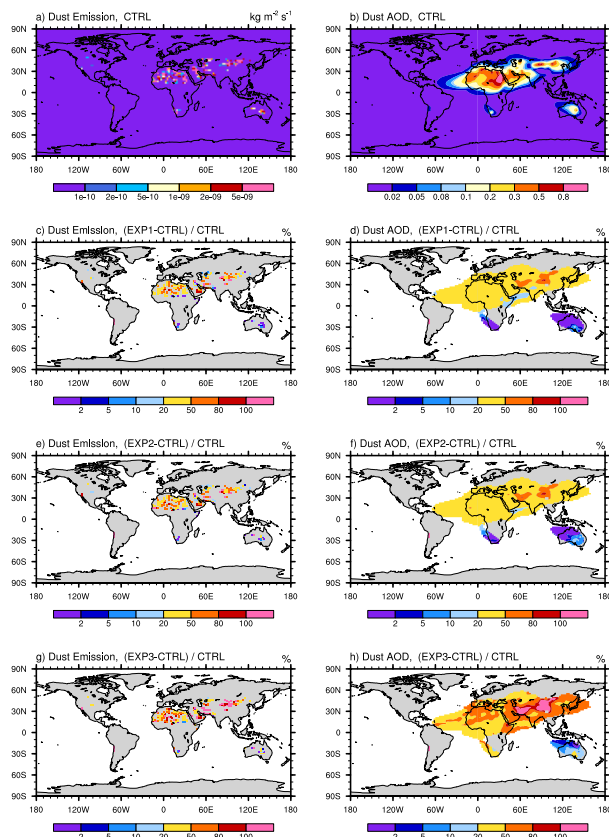


Figure 14. As in Fig. 14 but for dust emission and AOD. The threshold values for masking out relative differences in the lower rows are $1 \times 10^{-10} \text{ kg m}^{-2} \text{ s}^{-1}$ for emission and 0.01 for AOD.

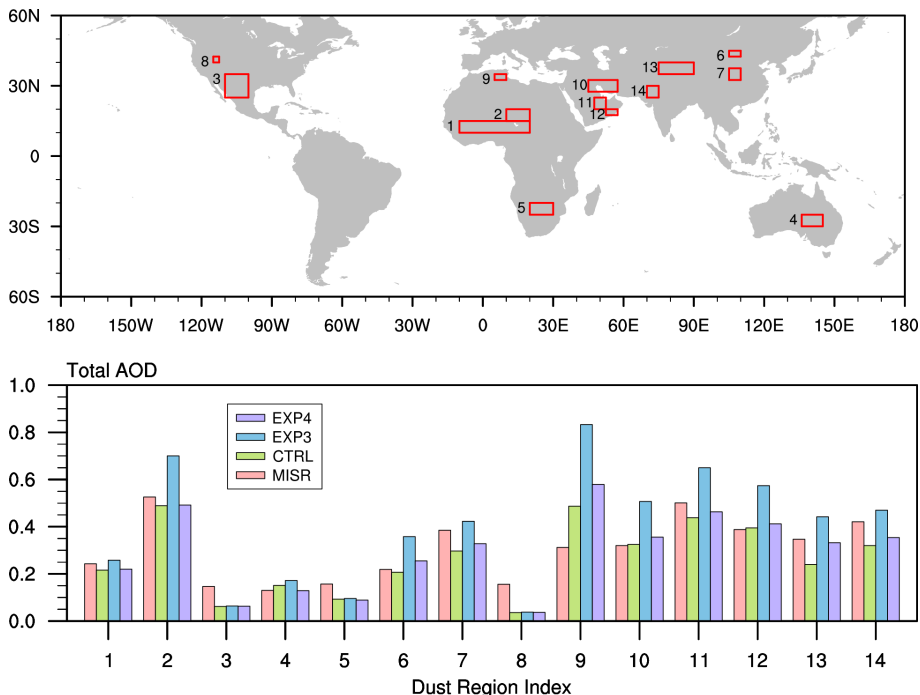


Figure 15. Satellite retrieved AOD from MISR (Multi-angle Imaging Spectro-Radiometer) and simulated regional average AOD at 14 major dust source regions (Tg yr^{-1}) for the year 2006. These regions were defined in the work of Zender and Kwon (2005) based on the dust source regions identified by Prospero et al. (2002) and data from Torres et al. (2002). Region definition and the data used to plot the lower panel are given Table 4.

Sub-grid wind-driven aerosol emissions in CAM5

K. Zhang et al.

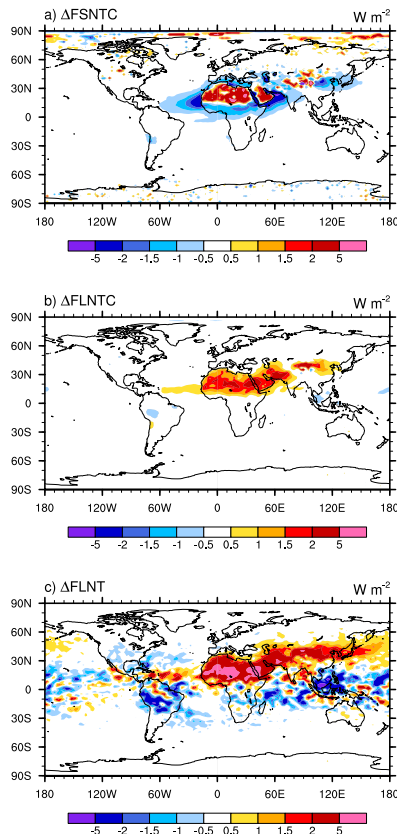


Figure 16. Differences of Top-Of-Atmosphere (TOA) radiative fluxes between simulations EXP3 and CTRL: **(a)** clear-sky shortwave radiative flux (FSNTC, positive downwards), **(b)** clear-sky longwave radiative flux (FLNTC, positive upwards), **(c)** all-sky longwave radiative flux (FLNT, positive upwards).

Sub-grid wind-driven aerosol emissions in CAM5

K. Zhang et al.

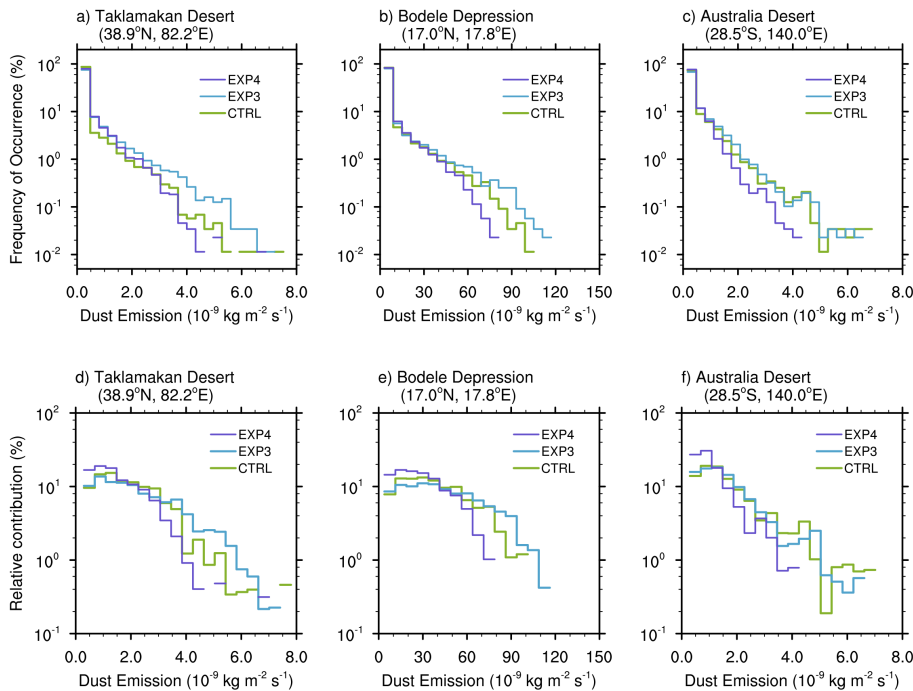


Figure 17. Upper row: frequency distribution of simulated dust emissions at three 2° lat \times 2° lon grid cells in the Taklamakan Desert, Bodele Depression and East Australia (from left to right). Lower row: the relative contribution of each emission range to the total emission at the same three grid cells. The results were derived from hourly emission fluxes of the year 2006.